

# PNG-UNITsims: Halo clustering response to primordial non-Gaussianities as a function of mass

Adrián Gutiérrez Adame<sup>1,2,3</sup> \*, Santiago Avila<sup>4,1,3</sup>, Violeta Gonzalez-Perez<sup>1,2</sup>, Gustavo Yepes<sup>1,2</sup>, Marcos Pellejero<sup>5,6</sup>, Mike S. Wang<sup>5</sup>, Chia-Hsun Chuang<sup>7,8</sup>, Yu Feng<sup>9</sup>, Juan Garcia-Bellido<sup>1,3</sup>, and Alexander Knebe<sup>1,2,10</sup>

<sup>1</sup> Departamento de Física Teórica, Universidad Autónoma de Madrid, 28049 Madrid, Spain

<sup>2</sup> Centro de Investigación Avanzada en Física Fundamental (CIAFF), Facultad de Ciencias, Universidad Autónoma de Madrid, ES-28049 Madrid, Spain

<sup>3</sup> Instituto de Física Teórica UAM-CSIC, c/ Nicolás Cabrera 13-15, Cantoblanco, 28049 Madrid, Spain

<sup>4</sup> Institut de física d'altres energies (IFAE) The Barcelona Institute of Science and Technology campus UAB, 08193 Bellaterra Barcelona, Spain

<sup>5</sup> Institute for Astronomy, University of Edinburgh, Royal Observatory Edinburgh, Blackford Hill, Edinburgh EH9 3HJ, United Kingdom

<sup>6</sup> Donostia International Physics Centre, Paseo Manuel de Lardizabal 4, 20018 Donostia-San Sebastian, Spain.

<sup>7</sup> Department of Physics and Astronomy, The University of Utah, 115 South 1400 East, Salt Lake City, UT 84112, USA

<sup>8</sup> Kavli Institute for Particle Astrophysics and Cosmology, Stanford University, 452 Lomita Mall, Stanford, CA 94305, USA.

<sup>9</sup> Berkeley Center for Cosmological Physics, University of California, Berkeley, CA 94720, USA

<sup>10</sup> International Centre for Radio Astronomy Research, University of Western Australia, 35 Stirling Highway, Crawley, Western Australia 6009, Australia

Submitted 20 December 2023

## ABSTRACT

This paper presents the PNG-UNITsims suite, which includes the largest full N-body simulation to date with local primordial non-Gaussianities (local PNG), the PNG-UNIT. The amplitude of the PNGs is given by  $f_{\text{NL}}^{\text{local}} = 100$ . The simulation follows the evolution of  $4096^3$  particles in a periodic box with  $L_{\text{box}} = 1 h^{-1} \text{Gpc}$ , resulting in a mass resolution of  $m_p = 1.24 \times 10^9 h^{-1} M_{\odot}$ , enough to finely resolve the galaxies targeted by stage-IV spectroscopic surveys. The PNG-UNIT has fixed initial conditions with phases also matching the pre-existing UNIT simulation with Gaussian initial conditions. The fixed and matched initial conditions reduce the simulation uncertainty significantly. In this first study of the PNG-UNITsims, we measure the PNG response parameter,  $p$ , as a function of the halo mass. Halos with masses between  $1 \times 10^{12}$  and  $5 \times 10^{13} h^{-1} M_{\odot}$  are well described by the universality relation, given by  $p = 1$ . For halos with masses between  $2 \times 10^{10}$  and  $1 \times 10^{12} h^{-1} M_{\odot}$  we find that  $p < 1$ , at a significance between 1.5 and  $3.1\sigma$ . Combining all the halos between  $2 \times 10^{10}$  and  $5 \times 10^{13} h^{-1} M_{\odot}$ , we find  $p$  consistent with a value of  $0.955 \pm 0.013$ , which is  $3\sigma$  away from the universality relation. We demonstrate that these findings are robust to mass resolution, scale cuts and uncertainty estimation. We also compare our measurements to separate universe simulations, finding that the PNG-UNITsims constraints outperform the former for the setup considered. Using a prior on  $p$  as tight as the one reported here for DESI-like forecast can result in  $f_{\text{NL}}$  constraints comparable to fixing  $p$ . At the same time, fixing  $p$  to a wrong value ( $p = 1$ ) may result in up to  $2\sigma$  biases on  $f_{\text{NL}}$ .

**Key words.** Cosmology – large-scale structure of Universe – Methods: numerical

## 1. Introduction

Primordial non-Gaussianities (PNG) provide a unique window into the Universe's dynamics during the inflationary era. One of the most widely studied models is that of local primordial non-Gaussianities, where the amplitude of the deviation from Gaussianity is typically parameterised using  $f_{\text{NL}}^{\text{local}}$  (Komatsu & Spergel 2001). In this paper, we only consider the local PNG, so we refer to this quantity simply as  $f_{\text{NL}}$  hereafter. Slow-roll single-field inflation predicts a nearly vanishing  $f_{\text{NL}}$  (Maldacena 2003; Creminelli & Zaldarriaga 2004). Therefore, detecting a significantly larger value ( $f_{\text{NL}} > 1$ ) would point to a more complex scenario, such as multi-field inflation (Lyth et al. 2003; Byrnes & Choi 2010; Pajer et al. 2013). Currently, the tightest constraints on  $f_{\text{NL}}$  come from the bispectrum measured for the anisotropies of the cosmic microwave background, with

$f_{\text{NL}} = -0.9 \pm 5.1$  (68% c.l.) (Planck Collaboration et al. 2020). However, this measurement is fundamentally limited by cosmic variance and it is not expected to reach the benchmark of  $\sigma(f_{\text{NL}}) = 1$ , even with the addition of polarisation data from the CMB (Baumann et al. 2009). Such a small error would allow us to detect or rule out most multi-field inflation models.

The most promising way to detect local PNG is through galaxy surveys, using the measurement of the so-called scale-dependent bias (Dalal et al. 2008; Slosar et al. 2008; Matarrese & Verde 2008). This method has been used during the last few years and has resulted in increasingly precise constraints (Slosar et al. 2008; Ross et al. 2012; Giannantonio & Percival 2014; Ho et al. 2015; Leistedt et al. 2014; Castorina et al. 2019; Cabass et al. 2022; Rezaie et al. 2024). The most precise measurement to date from spectroscopic surveys comes from SDSS-IV/eBOSS, which measured  $f_{\text{NL}} = -12 \pm 21$  (68% c.l.) (Mueller et al. 2022).

\* adrian.gutierrez@uam.es

Current spectroscopic galaxy surveys, such as DESI<sup>1</sup> and EUCLID<sup>2</sup>, are expected to reach a level of precision of  $\sigma(f_{\text{NL}}) \sim 5$  (Laureijs et al. 2011; Giannantonio et al. 2012; Sartoris et al. 2016; DESI Collaboration et al. 2016). The next generation of cosmological surveys is expected to reach  $\sigma(f_{\text{NL}}) < 1$  by combining the information coming from galaxy clustering with other probes, such as HI intensity mapping (LSST Science Collaboration et al. 2009; Yamauchi et al. 2014; Bacon et al. 2020; Kopana et al. 2024).

Interpreting current and future cosmological surveys requires the use of large simulations. They are routinely used for various purposes, from estimating covariance matrices (Manera et al. 2012; Avila et al. 2018; Zhao et al. 2021) to validating the analysis pipeline for the observational data (Avila et al. 2020; Alam et al. 2021; Rossi et al. 2020) and studying the theoretical models and observational aspects in a controlled environment (e.g. Ross et al. 2017; Avila et al. 2021; Chan et al. 2022; Riquelme et al. 2023). To date, there has been no adequate simulation to perform these studies in the presence of local PNG for stage IV spectroscopic surveys, given the limited mass resolution of the existing ones (Grossi et al. 2009; Desjacques et al. 2009; Pillepich et al. 2009; Hamaus et al. 2011; Scoccimarro et al. 2012; Wagner & Verde 2012).

To study the scale-dependent bias with the precision required by current galaxy surveys such as DESI ( $\sigma(f_{\text{NL}}) \sim 5$ ), the required simulation would need to have  $> 16\,000^3$  particles in a volume larger than  $(4\ h^{-1}\text{Gpc})^3$ . As this is extremely expensive to run, several techniques have been developed in recent years to increase the statistical significance of simulations. This increase can be obtained either by changing the way the initial conditions are generated (for example the fixed-and-paired technique proposed by Angulo & Pontzen 2016) or by using a set of approximate methods that are computationally less demanding and/or less expensive (Chartier et al. 2021; Ding et al. 2022; Kokron et al. 2022; DeRose et al. 2023).

First, we needed to clarify whether the fixed-and-paired technique could be used in the presence of local PNG, as fixing the Fourier modes' amplitudes breaks Gaussianity of the initial conditions. However, in Avila & Adame (2023), we demonstrated that this can also be used in the presence of local PNG to have a larger effective volume for simulations. In addition, in that work, we introduced a technique further to suppress the noise in the  $f_{\text{NL}}$  measurement. This suppression is achieved by matching the phases between two simulations with and without PNG, which removes much of the noise in the measured statistics associated with the cosmic variance. We use the results from Avila & Adame (2023) as a crucial ingredient in the following analysis.

This work presents the PNG-UNIT<sub>SIMS</sub> suite, which includes the largest simulation (in terms of number of particles) to date with non-Gaussian initial conditions, the PNG-UNIT. This simulation evolves  $4096^3$  dark matter particles within a cosmological volume of  $(1\ h^{-1}\text{Gpc})^3$ , resulting in a mass resolution of  $1.24 \times 10^9\ h^{-1}M_{\odot}$ . Most of the previously developed simulations with local-PNG were run with fewer particles, that is, by over a factor of 18 (e.g. Nishimichi et al. 2010; Baldauf et al. 2016; Biagetti et al. 2017; Coulton et al. 2023). Due to this low resolution, it was not possible to use these simulations to study the scale-dependent bias for low-mass halos and galaxies (i.e.  $M_{\text{halo}} \lesssim 1 \times 10^{13}\ h^{-1}M_{\odot}$ ). After the submission of this paper, Hadzhiyska et al. (2024) presented a new PNG simulations with

the same number of particles as the PNG-UNIT. However, these simulations have a volume of  $(2\ h^{-1}\text{Gpc})^3$ , resulting in a mass resolution  $\times 8$  times lower than the PNG-UNIT. Therefore, their objectives are different and complementary to the project presented in this paper.

The resolution of the PNG-UNIT simulation is enough to finely resolve (with more than  $\sim 100$  particles) the halos hosting the emission-line galaxies (ELGs) targeted by DESI and EUCLID ( $\sim 10^{11}\ h^{-1}M_{\odot}$ ) (Gonzalez-Perez et al. 2018; Yuan et al. 2024; Rocher et al. 2023; Reyes-Peraza et al. 2024). Other DESI tracers (BGS, LRG, QSO) are expected to probe even larger masses, which are also well resolved by this simulation (Yu et al. 2024; Rocher et al. 2023; Prada et al. 2023). The initial conditions of the PNG-UNIT are generated with amplitudes fixed to their expectation values and phases matched to one of the original UNIT simulations with Gaussian initial conditions (Chuang et al. 2019).

We first used the PNG-UNIT<sub>SIMS</sub> suite to constrain the non-Gaussian bias parameter,  $b_{\phi}$ , for mass-selected halos. This parameter controls how the clustering of halos, or any given tracer of the matter density field (cosmological tracer hereafter), responds to the presence of PNGs. However,  $b_{\phi}$  is completely degenerate with the amplitude of the non-Gaussianities measured by  $f_{\text{NL}}$  (Barreira 2022a). It is, therefore, crucial to have a good understanding of  $b_{\phi}$  if we aim to measure  $f_{\text{NL}}$  from data. Thus, understanding  $b_{\phi}$  from simulations will be essential.

An assumption is made for the mass function for halos where the mass only depends on the height of the density peak, namely,  $\nu = \delta_c/\sigma(M)$ , where  $\delta_c$  is the critical overdensity and  $\sigma(M)^2$  is the variance of the density field smoothed at mass  $M$ . On this basis, a theoretical prediction for  $b_{\phi}$  can be made as a function of the linear bias  $b_1$  (Dalal et al. 2008):

$$b_{\phi} = 2\delta_c(b_1 - 1). \quad (1)$$

This result is what is usually called the universality relation. Nevertheless, several works have shown that  $b_{\phi}$  may not be accurately described by that theoretical expectation (Slosar et al. 2008; Grossi et al. 2009; Hamaus et al. 2011; Scoccimarro et al. 2012; Wagner & Verde 2012; Biagetti et al. 2017). Moreover, it has been demonstrated that  $b_{\phi}$  may differ depending on the particular cosmological tracer (Barreira et al. 2020; Barreira 2022b).

In the literature,  $b_{\phi}$  has been constrained using not only the scale-dependent bias in simulations with PNG but also with other methods, namely the separate universe technique (Biagetti et al. 2017; Barreira et al. 2020; Barreira 2022a; Lazeyras et al. 2023). Although  $b_{\phi}$  can be measured very precisely with this approach, these simulations cannot validate non-Gaussian analysis tools of, for example, galaxy clustering, weak lensing statistics and cluster counts given they assume Gaussian initial conditions. Moreover, in this paper we find that the errors for the  $b_{\phi}$  obtained with the separate universe method may be underestimated.

In this work, we divided the halos into 12 pseudo-logarithmically spaced mass bins and studied their clustering by measuring their power spectrum. This statistic is sensitive to the product  $b_{\phi}f_{\text{NL}}$  through the scale-dependent bias (Dalal et al. 2008; Slosar et al. 2008). Here, we estimate the variance of the power spectrum for halos in PNG-UNIT from a set of fast mocks generated with FASTPM (Feng et al. 2016) with fixed initial conditions. We further improved the precision measuring  $b_{\phi}f_{\text{NL}}$  by matching the phases of the initial conditions. In the future, we plan to carry out a study of how  $b_{\phi}$  depends on the environment and the physics of galaxy formation in a non-Gaussian simulation.

<sup>1</sup> <https://www.desi.lbl.gov/>

<sup>2</sup> [https://www.esa.int/Science\\_Exploration/Space\\_Science/euclid\\_overview](https://www.esa.int/Science_Exploration/Space_Science/euclid_overview)

This paper is structured as follows. A brief review of the theory of galaxy clustering in the presence of local PNG is given in Section 2, focusing on the scale-dependent bias. In Section 3, we present the PNG-UNITsims suit of simulations developed for this study. In Section 4, we describe the methods employed for defining and relating the different mass bins, estimate the power spectrum variance, and apply the matching technique to improve the constraints on the PNG response parameters. In Section 5, we present and discuss our main findings, including the constraints on the  $b_\phi$  parameter for mass-selected halos. In Section 6, we study the convergence of our analysis with different sets of simulations and mass resolutions. The set of tests performed to ensure the robustness of our results are described in Section 7. In Section 8, we discuss how our results can be used as a prior for a DESI-like survey and how it would affect the constraints on  $f_{\text{NL}}$ . Finally, we present our conclusions in Section 9.

## 2. Theory

Dark matter halos trace the matter distribution, as these objects are assumed to form from high-density peaks. However, the gravitational collapse of dark matter halos is a non-linear and complex process. On quasi-linear scales, the complexities can be absorbed into a set of operators whose coefficients are called bias parameters (Bardeen et al. 1986; Desjacques et al. 2018). In the context of perturbation theory, the density contrast of halos and also other cosmological tracers, such as galaxies, can be written as a function of position and redshift:

$$\delta_h(\mathbf{x}, z) = \sum_O b_O(z) O(\mathbf{x}, z). \quad (2)$$

The operators,  $O$ , describe all the fields that may affect the matter density field, while  $b_O$  represents the bias parameters associated with each operator. If only local operators are considered, then the bias expansion can only contain terms with exactly two spatial derivatives of the potential, that is,  $O \propto \partial_i \partial_j \phi$  (see Desjacques et al. 2018, for an extensive review on the bias formalism). All the terms proportional to the matter density contrast  $\delta_m$  (e.g.  $\propto \delta_m^n$ ) are allowed in the local bias expansion given it is related with the potential through the Poisson equation ( $\nabla^2 \phi \propto \delta_m$ ). The leading order of Equation 2 can be expressed as:

$$\delta_h = b_1 \delta_m, \quad (3)$$

where  $\delta_h$  is the density field of halos,  $\delta_m$  is the density field of the matter distribution, and  $b_1$  is the linear bias. This expression is only valid on the purely linear regime, which typically is considered those below  $k_{\text{max}} \lesssim 0.1 h \text{ Mpc}^{-1}$ . By including more terms in Equation 2, the clustering of the halos can be modelled even in the mildly non-linear regime. This modelling is unnecessary as the effect of local PNG is mostly encoded in the largest scales (see §2.2). Hence, most of our analysis is focussed on the purely linear regime.

Using the linear bias,  $b_1$ , from Equation 3, the power spectrum of halos can be expressed in terms of the linear matter power spectrum,  $P_{m,m}(k, z)$ , as:

$$P_{h,h}(k, z) = \langle \delta_h \delta_h \rangle = b_1^2(z) P_{m,m}(k, z). \quad (4)$$

Below, we describe how PNG may arise from non-standard inflationary models (§2.1) and how it induces a scale dependence in the linear galaxy and halo bias (§2.2).

### 2.1. Primordial non-Gaussianities

The simplest inflationary models, such as single field slow-roll inflation, predict a nearly Gaussian spectrum of perturbations (Maldacena 2003; Creminelli & Zaldarriaga 2004). However, many models deviate from these assumptions, which may lead to large primordial non-Gaussianities (PNG) (e.g. Byrnes & Choi 2010; Ezquiaga et al. 2023). At first order, the amplitude of these deviations from Gaussianity is typically measured in terms of the first-order parameter  $f_{\text{NL}}$ . In the case of Gaussian fields, all the information is contained in the two-point function, and the higher-order statistics, such as the bispectrum and the trispectrum, are determined by the Wick theorem (Desjacques et al. 2018). However, this relation is modified in the presence of PNGs, and non-trivial contributions to the higher-order statistics may arise.

At first order, this  $f_{\text{NL}}$  term induces a non-vanishing component in the bispectrum. Specifically, by splitting the primordial potential into a Gaussian and a non-Gaussian part as  $\phi = \phi_G + \phi_{\text{NG}}$ , it can be shown that the leading order contribution to the bispectrum is given by:

$$\langle \phi_G \phi_G \phi_{\text{NG}} \rangle = (2\pi)^3 \delta_D(\mathbf{k}_1 + \mathbf{k}_2 + \mathbf{k}_3) \mathcal{B}_\phi(\mathbf{k}_1, \mathbf{k}_2, \mathbf{k}_3) \quad (5)$$

where  $\delta_D$  is the Dirac delta in 3D and  $\mathcal{B}_\phi(\mathbf{k}_1, \mathbf{k}_2, \mathbf{k}_3)$  is the primordial bispectrum. Depending on the shape induced in the primordial bispectrum, three types of PNGs have been traditionally considered: local, equilateral and orthogonal. Nevertheless, the landscape of possible non-Gaussianities is much richer and more complex.

This work focuses only on the local type, one of the simplest forms of PNGs. It can be described by the following parameterisation of the primordial gravitational potential (Salopek & Bond 1990; Komatsu & Spergel 2001):

$$\phi(\mathbf{x}) = \phi_G(\mathbf{x}) + f_{\text{NL}} \left( \phi_G(\mathbf{x})^2 - \langle \phi_G(\mathbf{x})^2 \rangle \right), \quad (6)$$

where  $\phi_G$  is the Gaussian primordial gravitational potential. The total primordial potential,  $\phi$ , is modified at quadratic order by a term proportional to  $f_{\text{NL}} \phi_G^2$  and now is non-Gaussian.

One finds that a non-vanishing component to the three-point function is induced from the expression for the local PNGs given in Equation 6. In this case, the bispectrum peaks in the squeezed limit ( $k_3 \ll k_1, k_2$ ) and is given by

$$\mathcal{B}_\phi(\mathbf{k}_1, \mathbf{k}_2, \mathbf{k}_3) = 2f_{\text{NL}} P_\phi(k_1) P_\phi(k_2) + (2 \text{ cyc. perm}), \quad (7)$$

where  $P_\phi(k)$  is the power spectrum of the primordial potential  $\phi$ , and (2 cyc. perm) are two cyclic permutations of the term  $P_\phi(k_1) P_\phi(k_2)$ .

The perturbations in the potential lead to a density contrast in the matter field through the Poisson equation. Then, the non-Gaussianities in the primordial potential are induced also in the matter density field. These fields can be related in the Fourier space via:

$$\delta(k, z) = \alpha(k, z) \phi(k, z), \quad (8)$$

where  $\alpha(k, z)$  is defined as

$$\alpha(k, z) = \frac{2D(z)}{3\Omega_{m,0}} \frac{c^2}{H_0^2} \frac{g(0)}{g(z_{\text{rad}})} k^2 T(k). \quad (9)$$

The parameter  $\Omega_{m,0}$  is the matter density parameter today,  $c$  is the speed of light, and  $H_0$  is the Hubble parameter today. The

transfer function  $T(k)$  is normalised such that  $T(k \rightarrow 0) = 1$ . The growth factor  $D(z)$  is also normalised to  $D(z = 0) = 1$ . The term  $\frac{g(z_{\text{rad}})}{g(0)}$  (with  $g(z) = (1+z)D(z)$ ) arises from the normalisation we assume for  $D(z)$  (Mueller et al. 2018). If the growth factor is normalised to  $(1+z)^{-1}$  during matter domination the term  $\frac{g(z_{\text{rad}})}{g(0)}$  can be omitted. For the cosmology described in Planck Collaboration et al. (2016) and we assume throughout the paper, we find that  $\frac{g(z_{\text{rad}})}{g(0)} = 1.275$ .

## 2.2. Scale-dependent bias

In the presence of local PNG, the leading-order term proportional to  $f_{\text{NL}}\phi$  in the bias expansion (Equation 2) gives

$$\delta_h(k, z) = b_1(z)\delta_m(k, z) + b_\phi f_{\text{NL}}\phi = \left[ b_1(z) + \frac{f_{\text{NL}}b_\phi(z)}{\alpha(k, z)} \right] \delta_m(k, z). \quad (10)$$

Here  $b_1$  is the linear bias, and  $\alpha(k, z)$  is given in Equation 9.  $b_\phi$  is the bias parameter associated with the  $\phi$  operator. This term only appears in the presence of PNG, as it is associated with the primordial bispectrum (Equation 7), which vanishes in the case of Gaussian initial conditions. The term  $\alpha$  introduces the  $1/k^2$  dependence of  $\delta_h$  on the scale  $k$ .

Using this new bias expansion, the power spectrum for dark matter halos, or any other biased tracer of the total matter density, can be computed similarly to Equation 4. The resulting halo power spectrum is given by

$$P_{h,h}(k, z) = \left[ b_1(z) + \frac{f_{\text{NL}}b_\phi(z)}{\alpha(k, z)} \right]^2 P_{m,m}(k, z). \quad (11)$$

The relationship between  $P_{h,h}(k, z)$  and  $P_{m,m}(k, z)$  now depends on the scale due to the term  $\alpha(k, z)$ , where the leading-order effect is proportional to  $1/k^2$ . This proportionality is what is commonly called the ‘scale-dependent bias’.

However, different values of  $f_{\text{NL}}$  may produce the same signal depending on the value of the bias parameter  $b_\phi$  as they are perfectly degenerate. This issue has already been discussed in the literature (Barreira 2022a).

The parameter  $b_\phi$ , by definition, represents the response of the abundance of halos to the presence of perturbations in the primordial potential  $\phi$ . As local PNG induces a mixing between the long-wavelength and short-wavelength perturbations (Equation 6), in the context of peak-background split theory (Kaiser 1984; Bardeen et al. 1986) it can be demonstrated that  $b_\phi$  can be thought of also as the response of the number density of halos to a rescaling of the amplitude of the primordial power spectrum (Desjacques et al. 2018; Barreira 2022c):

$$b_\phi = \frac{1}{\bar{n}_h} \frac{\partial \bar{n}_h}{\partial \log(f_{\text{NL}}\phi)} = \frac{1}{\bar{n}_h} \frac{\partial \bar{n}_h}{\partial \log \mathcal{A}_s}, \quad (12)$$

where  $\bar{n}_h$  is the mean number of halos and  $\mathcal{A}_s$  is the amplitude of the primordial scalar perturbations. Then, if a universal mass function is assumed, one can derive a theoretical prediction for the value of  $b_\phi$  (Dalal et al. 2008; Slosar et al. 2008; Desjacques et al. 2018):

$$b_\phi = 2\delta_c (b_1 - p). \quad (13)$$

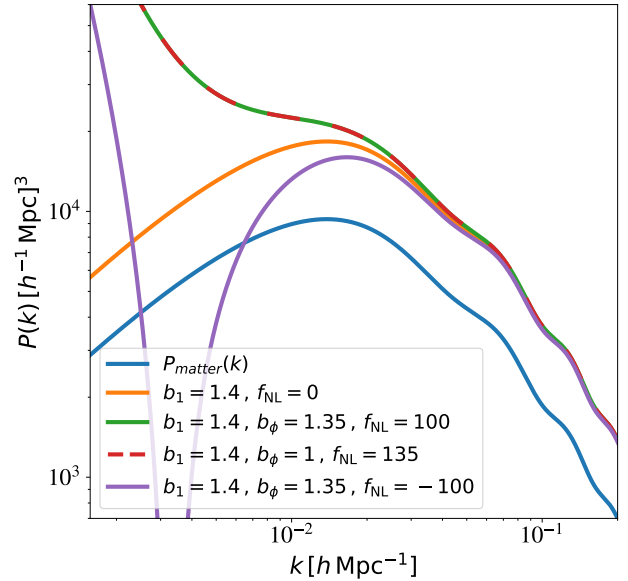


**Fig. 1.** Theoretical power spectrum obtained from Equation 11. The blue line shows the linear matter-matter power spectrum for the UNIT cosmology at  $z = 1$ . The  $b_1$  parameter is the same for all cases, and we chose it to be similar to the one expected for the DESI emission-line galaxies (ELGs) at that redshift (DESI Collaboration et al. 2016). The orange line corresponds to the case of a biased tracer with Gaussian initial conditions. The green line shows the effect of a non-Gaussian contribution with  $f_{\text{NL}} = 100$  and a PNG-response parameter  $b_\phi$  given by Equation 13 with  $p = 1$ . The red line displays how a different value of  $f_{\text{NL}}$  can lead to the same signal if the  $b_\phi$  parameter does not follow the universality relation. Red and green lines are on top of each other since the product  $b_\phi f_{\text{NL}}$  is the same. Finally, the purple line shows the kind of signal we expect in case  $b_\phi f_{\text{NL}} < 0$ .

Here,  $\delta_c = 1.686$  is the density threshold for the spherical collapse, and  $p$  may take different values depending on the population of objects under consideration. By assuming a universal mass function, then  $p = 1$  for all tracers of the matter distribution (Dalal et al. 2008; Slosar et al. 2008). This expression with  $p = 1$  is usually called the universality relation for  $b_\phi$  (noted as the universality relation hereafter).

Recent studies have shown that this relation does not always accurately describe the scale-dependent bias. For instance, Slosar et al. (2008) argued that for halos that have recently undergone a major merger process,  $b_\phi$  is better described by  $2\delta_c(b_1 - 1.6)$ , while Barreira et al. (2020) showed that for galaxies selected by their stellar mass, the relation with  $b_1$  is better described by  $2\delta_c(b_1 - 0.5)$ . Moreover,  $b_\phi$  may depend not only on the halo mass (through  $b_1$ ) but also on other properties such as the halo concentration (Lazeyras et al. 2023; Fondi et al. 2024).

In Figure 1, we present the expected power spectrum of dark matter halos at linear order in perturbation theory for different values of the non-Gaussian parameter,  $f_{\text{NL}}$ . We chose the value of  $b_1$  to be similar to the one expected for the emission-line galaxies (ELGs), a tracer sample targeted by the current galaxy surveys (Yu et al. 2024). For the Gaussian case, the halo power spectrum is just a shifted version of the matter-matter power spectrum in logarithmic scale, with the shift determined by the linear bias parameter  $b_1$ , as given by Equation 4. At large scales,

**Table 1.** Cosmological parameters of all UNITsims and PNG-UNITsims simulation suite (Planck Collaboration et al. 2016).

$\Omega_m$	0.3089
$\Omega_b$	0.0486
$\Omega_\Lambda$	0.6911
$h \equiv H_0/(100 \text{ km s}^{-1} \text{ Mpc}^{-1})$	0.6774
$\sigma_8$	0.8147
$n_s$	0.9667
$f_{\text{NL}}$	0, 100

the term proportional to  $b_\phi f_{\text{NL}}$ , which appears only for the case with local PNG, induces an enhancement for  $b_\phi f_{\text{NL}} > 0$  (red and green lines), and suppression if  $b_\phi f_{\text{NL}} < 0$  (purple line) of the power spectrum compared with the Gaussian case. When going to even larger scales, the term proportional to  $(b_\phi f_{\text{NL}})^2$  dominates, and an enhancement of the power spectrum is shown for both cases,  $b_\phi f_{\text{NL}} > 0$  and  $b_\phi f_{\text{NL}} < 0$ .

The scale-dependent bias is only sensitive to the product  $b_\phi f_{\text{NL}}$ . Because of this,  $f_{\text{NL}}$  cannot be extracted from this unless we have prior knowledge of  $b_\phi$  (Barreira 2022a), as illustrated in Figure 1, where the green and red lines show the same signal although the  $f_{\text{NL}}$  value is different.

### 3. Simulations

The UNITsims<sup>3</sup> simulation suite (Chuang et al. 2019) aims to model the large-scale structure of the Universe to validate theoretical models and analysis pipelines for extracting information about cosmological parameters in the current galaxy surveys. For this purpose, simulations need an effective volume equivalent to or larger than these surveys and a mass resolution high enough to resolve the dark matter halos hosting the targeted galaxies and tracers.

Most state-of-the-art simulations, including the UNIT simulation (§3.1), assume Gaussian cosmology and cannot be used directly to study the effect that PNG has on the distribution of large-scale structure at later cosmic times. To address this, we have developed the PNG-UNIT (Section 3.2), together with two lower-resolution full N-body simulations (LR-UNIT, §3.2.2) and a set of 100 fast N-body FASTPM mocks (§3.3). We developed another set of smaller simulations to perform further robustness tests on our analysis, which we discuss in section 3.4.

All simulations presented in this paper share the same cosmology (Planck Collaboration et al. 2016), as we summarise in Table 1. We outline the characteristics of the simulations in Table 2. Moreover, we focus our analysis on the snapshots at redshift  $z = 1.032$ .

Throughout the paper, we refer to the suite as PNG-UNITsims/UNITsims and to the 4096<sup>3</sup> particle simulation as PNG-UNIT/UNIT.

#### 3.1. The UNITsims

The UNITsims are a set of two pairs of state-of-the-art, dark matter-only, full N-body simulations with fixed-and-paired initial conditions (Angulo & Pontzen 2016; Chuang et al. 2019). Each of them tracks the evolution of 4096<sup>3</sup> particles in a periodic box with a side length of  $L = 1 h^{-1} \text{ Gpc}$  from redshift  $z = 99$  down to  $z = 0$ . The mass resolution is  $m_p = 1.24 \times 10^9 h^{-1} M_\odot$ , so the least massive halos expected to host galaxies targeted by current spectroscopic surveys, such as EUCLID and DESI, are well

resolved in these simulations (Cochrane et al. 2017; Gonzalez-Perez et al. 2018; Chuang et al. 2019; Knebe et al. 2022). In addition to the new simulations we run, we are also using in this work one of the original UNITsims, for reference, the one labelled FixAmpInvPhase\_001.

The initial conditions were set using the second-order Lagrangian Perturbation Theory (2LPT), implemented in FASTPM<sup>4</sup> (Feng et al. 2016). The required initial power spectrum was computed using the Boltzmann solver CAMB<sup>5</sup> (Lewis et al. 2000).

The dark matter particles were evolved using the N-body code L-GADGET2 (Springel 2005). This code uses a Tree-PM algorithm to compute the forces between particles by splitting the Newtonian potential into long-range and short-range components. We employed the non-public version of the code L-GADGET-2 as it is highly optimised regarding memory usage. This code has been widely used for generating many large-volume and high-resolution simulations such as the MILLENNIUM run (Springel et al. 2005) and the MULTIDARK suite (Klypin et al. 2016). The Plummer softening length was set to  $\epsilon = 6 \text{ kpc}/h$  and then the particles were evolved from  $z = 99$  down to  $z = 0$ , stored in a total of 129 snapshots logarithmically spaced in the scale factor.

Dark matter halos were identified using the publicly available code ROCKSTAR<sup>6</sup> (Behroozi et al. 2012). This code uses the particles' 6D phase space information to identify the dark matter halos. These structures are identified as having at least 20 particles per halo. We used CONSISTENT TREES to track their merger histories and build the merger trees. More details regarding these simulations can be found in Chuang et al. (2019).

#### 3.2. The PNG-UNITsims

We developed the new PNG-UNITsims suite for this paper with the same features as the original UNITsims simulations but with non-Gaussian initial conditions. Specifically we set  $f_{\text{NL}} = 100$ . The suite consists of a high-resolution simulation (§3.2.1), a lower resolution version of it (Section 3.2.2) and a set of 100 fast mocks generated with FASTPM, half of them with  $f_{\text{NL}} = 0$  and the other half with  $f_{\text{NL}} = 100$  (§3.3).

To generate the initial conditions of all of these simulations, we have used the FASTPM code. In the first place, the initial conditions are generated for  $\phi$  in the same way as if the simulation were Gaussian. Indeed, at this point, the amplitudes of the Fourier modes can be fixed to their expectation value as in Angulo & Pontzen (2016). Then, to induce the local PNGs, the primordial potential is computed from the density field using Equation 8 and then the transformation given in Equation 6 is applied. This procedure is detailed and validated in Avila & Adame (2023).

##### 3.2.1. The PNG-UNIT

The PNG-UNIT simulation is the main product of this work as it is the largest full N-body simulation in terms of number of particles with primordial non-Gaussianities to date. It is a dark matter-only, full N-body simulation with local primordial non-Gaussianities. As the original UNIT simulation, it tracks the evolution of 4096<sup>3</sup> particles in a periodic box with a side length of  $L = 1 h^{-1} \text{ Gpc}$  from redshift  $z = 99$  down to  $z = 0$ . The details are shown in Table 2. Given the large volume and the high

<sup>4</sup> <https://github.com/fastpm/fastpm>

<sup>5</sup> <https://camb.info/>

<sup>6</sup> <https://bitbucket.org/gfcanford/rockstar/src/main/>

<sup>3</sup> <http://www.unitsims.org/>

**Table 2.** Characteristics of the main simulations used throughout the present paper.

	UNIT	PNG-UNIT	LR-UNIT	FASTPM mocks
Code	L-Gadget 2	L-Gadget 2	L-Gadget 2	FASTPM
$N_{\text{particles}}$	4096 <sup>3</sup>	4096 <sup>3</sup>	2048 <sup>3</sup>	2048 <sup>3</sup>
$m_p$ ( $h^{-1} M_{\odot}$ )	$1.24 \times 10^9$	$1.24 \times 10^9$	$9.97 \times 10^9$	$9.97 \times 10^9$
$f_{\text{NL}}$	0	100	0 and 100	0 and 100
Halo finder	Rockstar	Rockstar	Rockstar	FoF
Softening length ( $h^{-1}$ kpc)	6.1	6.1	12.2	244.14*

**Notes.** We refer to the simulations as PNG-UNIT/UNIT while we leave the names PNG-UNIT<sub>SIMS</sub>/UNIT<sub>SIMS</sub> for the simulation suites. From top to bottom: the gravity solver, the number of dark matter particles, the particle mass, the values of  $f_{\text{NL}}$  set in the initial conditions, the halo finder and the softening length. All the simulations have a box size of  $L_{\text{box}} = 1 h^{-1}$  Gpc. The cosmological parameters and the input power spectrum are the same (except for  $f_{\text{NL}}$ ) between all the simulations. \* FASTPM is a particle-mesh code, so the cell size gives the force resolution, and this is the number we report in the table as softening length for FASTPM.

mass resolution, this simulation is a unique laboratory to validate models of galaxy clustering in the presence of local PNG.

The value of  $f_{\text{NL}}$  used for generating the initial conditions is set to  $f_{\text{NL}} = 100$ . This large value of  $f_{\text{NL}}$  is already ruled out by Planck at  $\sim 20\sigma$  (Planck Collaboration et al. 2020). However, we wanted a strong signal from the scale-dependent bias to understand this effect better. With a more realistic  $f_{\text{NL}}$ , given our limitation in scales with minimum wavenumber  $k_{\text{min}} = k_f = 0.006 h \text{Mpc}^{-1}$  (where  $k_f$  is the fundamental wavenumber), we would not be able to detect the PNG signal in the halo power spectrum.

In addition, the initial conditions of the PNG-UNIT were generated using the fixed-and-matched technique described in Avila & Adame (2023). The amplitudes were set to the expectation value as in Angulo & Pontzen (2016). This method can be safely applied also in simulations with local primordial non-Gaussianities as demonstrated in Avila & Adame (2023). Then, the phases were chosen to be the same as in the reference Gaussian UNIT simulation. The N-body code and the halo finder were run using the same configuration as for the UNIT<sub>SIMS</sub>. We focus our analysis on the snapshot at redshift  $z = 1$ .

### 3.2.2. The LR-UNIT simulations

In addition to the high-resolution simulation presented above, for the purposes of this paper, we have developed two new lower-resolution versions of the previous ones (with  $f_{\text{NL}} = 0$  and  $f_{\text{NL}} = 100$ ). The primary purpose of these LR-UNIT simulations is to understand the effects of mass resolution better (see §6.1). For this reason, we use the same configuration as the high-resolution simulations. The only difference is the resolution (see Table 2).

As we used the same code and seed to generate the initial conditions, all the long-wavelength modes were set to the same values as in the high-resolution simulations. Thus, the same region of the Universe is modelled in these low-resolution simulations, and the same structures can be identified in both sets of simulations.

### 3.3. FASTPM mocks

We have also generated a set of 100 fast mocks using FASTPM (Feng et al. 2016). These mocks were split into two sets of 50: one set had Gaussian initial conditions ( $f_{\text{NL}} = 0$ ) while the other set had non-Gaussian initial conditions ( $f_{\text{NL}} = 100$ ).

FASTPM is a code that combines perturbation theory with a particle-mesh (PM) approach to quickly generate cosmological

simulations at the cost of poor resolution of the short-wavelength modes. This code is particularly useful for generating many simulations quickly, which can be used, for example, for estimating covariance matrices at a low computational cost. In this work, we use FASTPM mocks to estimate the variance of the power spectrum of the halos in simulations with fixed initial conditions as well as for obtaining the correlation coefficients required by the matching technique as we discuss in Section 4.3.

Each simulation box contains 2048<sup>3</sup> dark matter particles within a cosmological volume of  $1 (h^{-1} \text{Gpc})^3$ , the same volume as the UNIT simulation. The mass resolution is  $m_p = 9.97 \times 10^{10} h^{-1} M_{\odot}$ , which is 8 times coarser than the high-resolution simulations (same resolution as LR-UNIT simulations) but still sufficient for this work. The force resolution in the PM approach is given by the grid size used to compute the potential and the forces. We use a regular grid of 4096<sup>3</sup> cells, giving a spatial resolution of  $244.14 h^{-1} \text{kpc}$ .

Following the same procedure as the full N-body simulations, the initial conditions were set at  $z = 99$  using second-order Lagrangian perturbation theory with fixed amplitudes. The particles were then evolved to  $z = 1$  using 100 linearly spaced timesteps.

We use the friends-of-friends (FoF) algorithm to generate the halo catalogues, which is implemented by default in FASTPM. The linking length is set to the standard value of  $l_l = 0.2 l_p$ , where  $l_p$  is the mean interparticle distance.

The difference between the halo finder used for the FASTPM and the PNG-UNIT catalogues leads to a different mass definition for dark matter halos. This issue is addressed in Section 4.1.

### 3.4. Supporting simulations

In addition to the PNG-UNIT and the FASTPM mocks presented above, we developed an additional set of simulations mainly aimed at checking the robustness of our results. We want to check if the results obtained from fitting  $b_{\phi}$  in Equation 11 are consistent with measuring  $b_{\phi}$  using the separate universe technique (see §6.2). Hence, the set of simulations is split into two groups: high-resolution (HR) and low-resolution (LR) separate universe simulations.

Each group consists of 3 simulations with 512<sup>3</sup> dark matter particles within a periodic cubic box of size  $L_{\text{box, HR}} = 67.5 h^{-1} \text{Mpc}$  and  $L_{\text{box, LR}} = 250 h^{-1} \text{Mpc}$  for the high-resolution and low-resolution groups respectively. This configuration leads to a mass resolution which is eight times better and eight times worse, respectively, compared to the baseline UNIT<sub>SIMS</sub>. Again,

the fiducial cosmology is the same as the one of the UNIT simulations, summarised in Table 1. Following a similar procedure as shown in Barreira (2022a), we produced three simulations with the same initial conditions but varied the  $\mathcal{A}_s$  (or equivalently  $\sigma_8$ ) by 5%. This variation allows us to numerically measure  $b_\phi$  by computing the derivative (Equation 22), as we discuss in Section 6.2.

For all these simulations, we evolved the particles using the L-GADGET 2 code, as in the case of the high-resolution simulations and we set the Plummer softening length to 1/40 times the mean interparticle distance, which varies depending on the mass resolution of the simulations.

### 3.5. Compared halo mass functions

Figure 2 shows the cumulative mass function of the halos from the PNG-UNIT and LR-UNIT simulations. The mass function has been calculated from  $2.48 \times 10^{10} h^{-1} M_\odot$  (20 times the particle mass in PNG-UNIT) up to  $1 \times 10^{15} h^{-1} M_\odot$  in 50 logarithmically spaced bins. We find that the low-resolution simulations converge to the high-resolution ones at  $< 5\%$  for  $M \sim 100 m_{\text{part}}^{\text{LR}}$ , with  $m_{\text{part}}^{\text{LR}}$  being the particle mass of the lower resolution simulation. The shaded area represents the threshold of 20 particles per halo, below which the mass of the halos is unreliable in the low-resolution simulations.

The first thing we remark is that the mass function of the FASTPM mocks differs significantly from the ones from the full N-body simulations. The reason is that the mass definition is different since for the FASTPM mocks, halos were identified with a FoF algorithm while we used ROCKSTAR for the halos in the other simulations. This difference highlights the need for establishing a correspondence between the full N-body halos and the FASTPM halos. We devote Section 4.1 to this task.

We checked that the differences in the mass function are mainly due to the different halo-finding algorithms by running Rockstar on one of FASTPM mocks. Running both halo finders on the same FASTPM mock, we find that for high masses, the mass function matches that of the full N-body simulations, while we find a deficit in the number of low-mass halos; this is probably due to differences in the resolution of the forces between the two approaches.

Moreover, we find an increment of the high-mass halos in the  $f_{\text{NL}} = 100$  simulations with respect to the Gaussian ones. This increment was expected due to the change of the probability density function (PDF) of  $\delta$  due to the presence of local PNG (Matarrese et al. 2000; LoVerde et al. 2008).

The Gaussian UNIT simulation has an excess of low mass halos compared with the other simulations due to an issue with the initial conditions affecting the older version of the FASTPM code used to produce that simulation. This problem produced an excess power in the power spectrum of the initial conditions at scales between  $k_{\text{nyquist}}/4$  and  $k_{\text{nyquist}}/2$  of the order of 10%. This results in an overproduction of halos of the same order of  $\sim 10\%$  and explains the differences between the UNIT and the PNG-UNIT simulations at the mass function level. However, this does not significantly affect the halo clustering measurements compared to the low-resolution simulations, as we explain in Section 6.1.

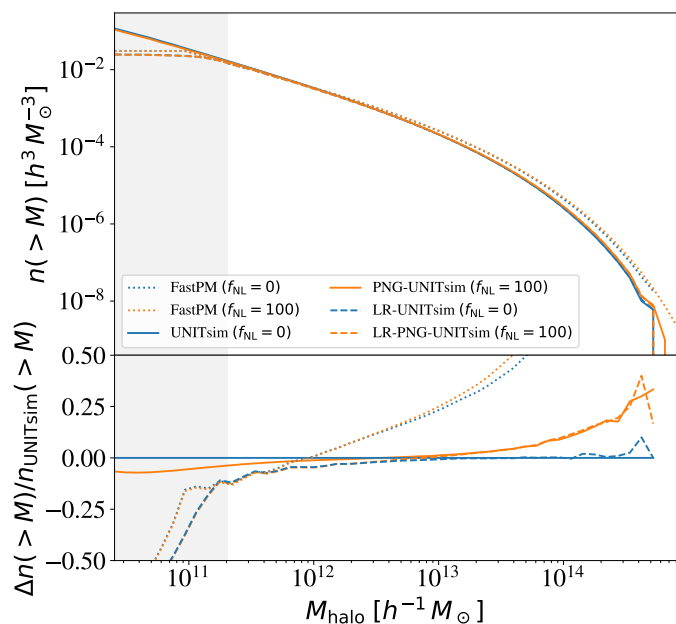


**Fig. 2.** Halo mass functions for the simulations described in Section 3 (top). Ratio of halo mass functions relative to the Gaussian UNIT simulation as the reference (bottom). Shaded areas represent the  $M = 20m_{\text{part}}^{\text{LR}}$  mass threshold for the low-resolution simulation. The minimum mass shown here represents the 20 particle limit for the higher resolution simulations.

## 4. Uncertainty of the Power Spectrum in simulations with fixed-and-matched initial conditions

In this work, we study the PNG parameters  $b_\phi$  and  $f_{\text{NL}}$  as a function of halo mass. We measure them using the scale-dependent bias induced by PNG in the halo power spectrum (Section 2.2). The dark matter auto-power spectra of the simulations are obtained by interpolating the particles onto a regular grid with  $N = 512^3$  cells using a cloud-in-cell (CIC) scheme (Hockney & Eastwood 1981) with a  $k$ -bin width equivalent to the fundamental wavenumber of the box ( $k_f = 2\pi/L_{\text{box}} = 0.00628 h \text{ Mpc}^{-1}$ ). We have used the PYTHON library NBODYKIT<sup>7</sup> (Hand et al. 2018) for this task. The halo power spectrum is computed similarly but using the halo positions instead of the dark matter particles. In addition, we use a large set of fast mocks to estimate the variance in the power spectrum from the full N-body simulations. This approach allows us to consider the variance suppression due to the initial conditions (see §4.2). However, fundamental differences exist between the fast mocks and the PNG-UNIT. The main differences are how the halos are defined and the mass resolution of the simulations. We now discuss how to connect the halos (and, hence, the measured power spectrum) from the full N-body simulation with the corresponding ones from the fast mocks.

### 4.1. Adapting FASTPM mass bins to UNITSIM

Throughout this work, we only consider main halos, which are not substructures of a larger halo. For simulations where we run ROCKSTAR (see Table 2), the halo mass is estimated from a spherical overdensity up to the threshold of  $\Delta = 200\rho_c$ , where  $\rho_c$  is the critical density (Behroozi et al. 2012). For the FASTPM mocks,

<sup>7</sup> <https://nbodykit.readthedocs.io/en/latest/>

the halo mass is the sum of the particle mass of its FoF components. This mass definition leads to some differences when choosing the mass bins. The edges of the mass bins are chosen with pseudo-logarithmic spacing for UNIT, as summarised in Table 3.

The mass definitions in the full N-body simulations differ significantly from those for the fast mocks. To relate halos between these two approaches, we aim to reproduce simultaneously the clustering and the abundances of the UNIT halos with the FASTPM mocks. To this end, for each mass bin of the UNITsim, we consider a maximum mass for the halos in the FASTPM mocks and select the following  $N$  most massive halos to recover the UNIT number density. Using a least-squares algorithm, we find the optimal maximum mass for FASTPM that reproduces the UNIT power spectrum for  $k < 0.1 h \text{Mpc}^{-1}$ . We take the minimum and the maximum mass from the resulting bins and apply these cuts for the  $f_{\text{NL}} = 100$  simulations.

Figure 3 shows the power spectrum of FASTPM compared to that from the PNG-UNIT. The lines are the power spectrum computed for the PNG-UNIT for the mass bins from Table 3. The shaded areas are the mean and the standard deviation of the power spectra obtained from the FASTPM mocks using the above procedure.

There are no halos in the fast mocks for the three lowest-mass bins since the mass resolution is not high enough to resolve them. In the case of the two most massive bins, although we can recover the clustering, we cannot simultaneously recover the abundance. This problem is associated with the mass and bias function differences due to the distinct halo finders used (see Figure 2). In addition, the power spectra for the three most massive bins in the PNG-UNIT are very noisy since the number density is very low ( $n < 10^{-5} h^3 \text{Mpc}^{-3}$ ).

#### 4.2. Variance estimation from fast mocks for fixed simulations

We focus now on the computation of the covariance matrix for the power spectrum. In the linear regime, the covariance matrix can be assumed to be nearly diagonal. Therefore, the expected variance for a Gaussian density field can be computed following the expression (Feldman et al. 1994):

$$\sigma_S^2(k) = \frac{4\pi^2}{Vk^2\Delta k} \left( P(k) + \frac{1}{\bar{n}} \right)^2, \quad (14)$$

where  $P(k)$  is the power spectrum,  $\Delta k$  is the width of the power spectrum bins,  $\bar{n}$  is the mean number density of tracers, and  $V$  is the simulation volume. We refer to this quantity as  $\sigma_S(P(k))$ , the standard error.

As the initial conditions of the simulations were fixed to their expectation value (§3), a considerable suppression is expected with respect to Equation 14, particularly relevant for the largest scales (Angulo & Pontzen 2016; Villaescusa-Navarro et al. 2018; Avila & Adame 2023; Maion et al. 2022).

Our approach is to estimate directly  $\sigma(P(k))$  as the standard deviation of the FASTPM mocks and apply them for the parameter estimation using the full N-body simulation. However, this quantity is still noisy due to the limited number of mocks available to calculate it. Moreover, we still have a problem obtaining this quantity for bins beyond the resolution limit of the FASTPM mocks.

Therefore, we propose fitting the ratio  $\sigma(P(k))/P(k)$  with a smooth function in order to get a less noisy estimate of the errors. For that, we measure  $\sigma(P(k))/P(k)$  directly from the FASTPM mocks (for the mass bins 3-10 from Table 3 whose power spectra

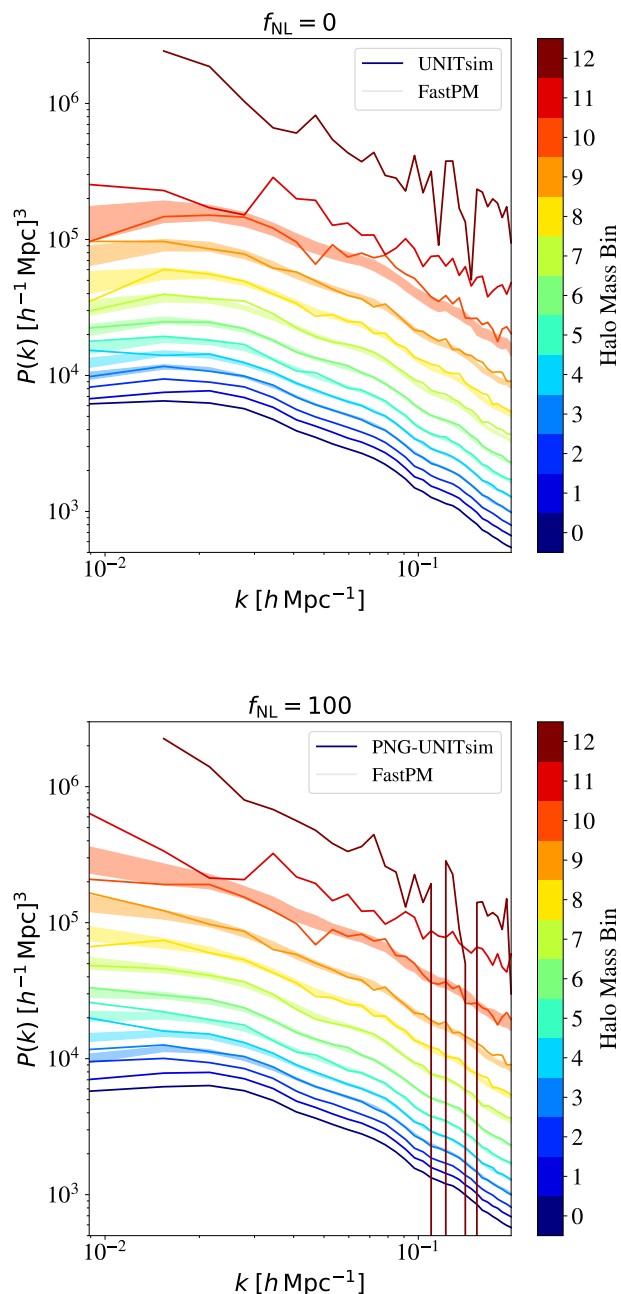


**Fig. 3.** Solid lines represent the power spectrum of PNG-UNIT halos within the different halo mass bins (see Table 3 for the mass ranges). Shaded regions show the standard deviation around the mean power spectrum of the FASTPM mocks, generated using halos in mass bins that reproduce the clustering and the abundance of the N-body simulation (see Section 4.1). There are no halos in the two lowest-mass bins (1 and 2, shown in dark blues) in the FASTPM mocks since the mass resolution is not high enough to resolve them. The top panel shows the  $f_{\text{NL}} = 0$  case, and the bottom panel shows the  $f_{\text{NL}} = 100$  one.

are consistent with the ones coming from the PNG-UNIT) and fit it to the following ansatz that we find convenient after several trials of different functional forms:

$$\frac{\sigma(P(k))}{P(k)} = f(k; a, b, c) = a \left( 1 + \frac{1}{1 + b \exp(-ck)} \right). \quad (15)$$



**Table 3.** PNG parameters derived for halos in different mass bins.

Bin	Mass Range ( $h^{-1} M_{\odot}$ )	$b_{\phi} f_{\text{NL}}$ $\sigma_{S, \text{UNIT}}$	$b_{\phi} f_{\text{NL}}$ $\sigma_{F+M}$	$f_{\text{NL}} (p = 1)$ $\sigma_S$	$\rho$	$f_{\text{NL}} (p = 1)$ $\sigma_{F+M}$	$p$ $\sigma_{F+M}$
0	$(2, 5] \times 10^{10}$	$16 \pm 55$	$-37.9 \pm 7.0$	$30 \pm 130$	0.703	$94 \pm 10$	$0.993 \pm 0.021$
1	$(5, 10] \times 10^{10}$	$4 \pm 54$	$7.4 \pm 9.1$	$-90 \pm 400$	0.703	$-55 \pm 45$	$0.938 \pm 0.027$
2	$(1, 2] \times 10^{11}$	$2 \pm 63$	$48 \pm 12$	$490 \pm 600$	0.703	$409 \pm 74$	$0.892 \pm 0.035$
3	$(2, 5] \times 10^{11}$	$-8 \pm 69$	$67 \pm 11$	$140 \pm 150$	0.807	$138 \pm 25$	$0.946 \pm 0.034$
4	$(5, 10] \times 10^{11}$	$-15 \pm 83$	$128 \pm 18$	$157 \pm 100$	0.767	$138 \pm 18$	$0.895 \pm 0.055$
5	$(1, 2] \times 10^{12}$	$10 \pm 100$	$168 \pm 29$	$112 \pm 68$	0.736	$111 \pm 15$	$0.951 \pm 0.086$
6	$(2, 5] \times 10^{12}$	$-50 \pm 110$	$244 \pm 26$	$79 \pm 52$	0.706	$104 \pm 11$	$0.973 \pm 0.077$
7	$(5, 10] \times 10^{12}$	$-110 \pm 140$	$307 \pm 43$	$60 \pm 46$	0.665	$85 \pm 12$	$1.16 \pm 0.13$
8	$(1, 2] \times 10^{13}$	$-230 \pm 160$	$476 \pm 90$	$54 \pm 39$	0.635	$93 \pm 13$	$1.11 \pm 0.27$
9	$(2, 5] \times 10^{13}$	$50 \pm 260$	$630 \pm 120$	$89 \pm 43$	0.605	$88 \pm 16$	$1.26 \pm 0.35$
10	$(5, 10] \times 10^{13}$	$-2138 \pm 940$	$1020 \pm 290$	$-58 \pm 57$	0.564	$85 \pm 26$	$1.53 \pm 0.93$
11	$(1, 2] \times 10^{14}$	$-1796 \pm 1800$	$880 \pm 600$	$-70 \pm 100$	0.534	$48 \pm 36$	$3.8 \pm 1.9$
12	$(2, 5] \times 10^{14}$	$-548 \pm 1800$	$-4230 \pm 740$	$-15 \pm 79$	0.504	$-145 \pm 27$	$22.4 \pm 2.4$

**Notes.** The first column shows the ID of each bin. The second column presents the mass range for the halos as taken from the PNG-UNIT (Section 4.1). In the third column, we show the measurements we get for the product  $b_{\phi} f_{\text{NL}}$  using the standard errors ( $\sigma_S(P(k))$ ) for the Gaussian UNIT simulation. In the fourth column, we present the results of  $b_{\phi} f_{\text{NL}}$  after applying the matching between the PNG-UNIT and the UNIT simulations (Section 5.2). The fifth column provides the  $f_{\text{NL}}$  values obtained from the PNG-UNIT simulation using standard errors and assuming the universality relation,  $p = 1$ , in Equation 13. The sixth column shows the Pearson correlation coefficient,  $\rho$ , assumed for each halo mass bin. These values have been obtained after a linear regression of the quantities measured for bins 3–10, as described in Section 4.3. For bins 0–2, we use instead the mean of the measurements of  $\rho$ , which is  $\bar{\rho} = 0.703$ , as discussed in the same section. In the seventh column, we present the results when applying the reduced errors derived from the FASTPM mocks and matching them with the Gaussian simulation (Section 5.3). The last column displays the values of  $p$  obtained from Equation 13, which are used to correct the value of  $f_{\text{NL}}$  in the fifth column to the input value (Section 5.4). We find that the error estimates are not robust for the bins in grey and may lead to biases in the conclusions about  $b_{\phi}$ . Therefore, as discussed in Section 5.2, they are not considered for subsequent analyses.

In Figure 4, we show the fits of the FASTPM mocks to the previous expression in solid lines. To extrapolate  $\sigma(P(k))/P(k)$  beyond the mass resolution of the fast mocks, we fitted the three parameters  $a$ ,  $b$  and  $c$  from Equation 15 we obtained as a function of the mass. For parameter  $a$ , we use an exponential function; for parameters  $b$  and  $c$ , we use a polynomial of order two as a function of  $\log_{10} M_{\text{halo}}$ . The extrapolations are shown in Figure 4 as dashed lines.

We will now adopt by default the errors coming from the fit to Equation 15 for bins 3-10 and the extrapolation for bins 0-2 and 11-12. Nevertheless, we checked the impact of this assumption, as detailed in Section 7.1.

#### 4.3. Reducing the errors using fixed-and-matched simulations

When two simulations share the same set of random phases in their initial conditions, their cosmic variance is highly correlated even if they have different cosmologies. Here, we discuss how we take advantage of the correlated noise from two simulations with different  $f_{\text{NL}}$  to constrain the PNG bias parameters with high precision. This noise reduction technique is what we call ‘matching the simulations’.

The initial conditions for an N-body simulation are a realisation of a Gaussian random field generated from the power spectrum of primordial perturbations. There are two degrees of freedom: the amplitude of the perturbations, whose expected value is determined by the power spectrum, and the phase of those perturbations, which are randomly uniformly distributed between 0 and  $2\pi$ . This stochasticity in the generation of the initial conditions (ICs), usually called the cosmic variance, leads to some degree of noise when measuring quantities from simulations in the same way as we expect it to be in the real Universe. The level of

noise can be suppressed, for example, by fixing the amplitudes of the modes to their expectation value (Angulo & Pontzen 2016).

The idea presented in Avila & Adame (2023) is that if the initial conditions of two simulations share the same stochastic part, that is, the same random phases and the same deviations in the amplitude from their corresponding average (in case they do not have fixed ICs), then the cosmic variance is expected to be highly correlated. Hence, we could cancel out much of the noise affecting measurements by matching that simulation with an existing one with the same ICs but a different cosmology.

We applied this in Avila & Adame (2023) for measuring  $f_{\text{NL}}$ , where only three ingredients were needed for the measurement: the value of  $f_{\text{NL}}$  obtained from the Gaussian simulation, the same quantity from the non-Gaussian simulation and the correlation coefficient  $\rho$  between both simulations. In that study, we used a set of full N-body simulations with matched ICs (i.e. the same stochastic part) to measure  $\rho$ .

In this study, we adopt an alternative strategy by leveraging only two simulations, UNIT and PNG-UNIT, along with a suite of computationally efficient mocks to estimate  $\rho$ . This approach circumvents the need for an extensive series of full N-body mocks, which would be impractically demanding on computational resources at this mass resolution. More precisely, we determine  $b_{\phi} f_{\text{NL}}$  for each bin within each FASTPM realisation and then calculate the Pearson correlation coefficient to obtain  $\rho$ .

We find that the measurements of  $b_{\phi} f_{\text{NL}}$  correlate more when the mass of the halos is lower. This finding may be because the lower the mean mass of the bins, the higher the number of halos included, and therefore, the less noisy the power spectrum measurement. We performed a linear fit of this  $\rho$  as a function of the mass to reduce the noise associated with the measurement of

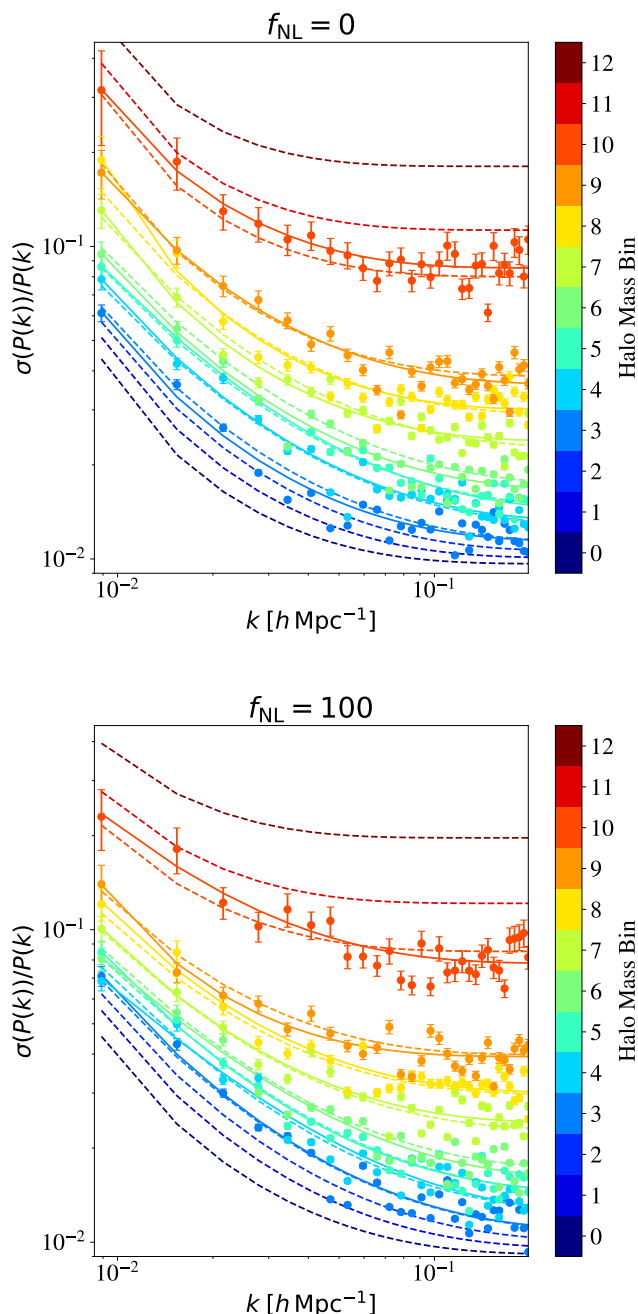


**Fig. 4.** Variance over mean power spectrum for each halo mass bin (indicated by colour with the mass ranges defined in Table 3). Markers with error bars show the data taken directly from the FASTPM mocks, while solid lines show results obtained by fitting these curves to Equation 15. The extrapolation to each mass bin as described in Section 4.2 is shown in dashed lines.

this quantity<sup>8</sup>. The results of the linear fit are reported in Table 3. However, studying the evolution of the correlation with mass in depth is beyond the scope of this paper.

Thus, we are left with the question of obtaining the correlation coefficients for those bins where we do not have FASTPM mocks. One possibility is to use the values obtained from the lin-

<sup>8</sup> The values of  $\rho$  measured for bins 3–9 are: 0.852, 0.763, 0.614, 0.781, 0.748, 0.468, 0.696

ear regression as a function of bin mass. This regression would give us a correlation coefficient of  $\rho \sim 0.9$  for the less massive halo bins (i.e. bins 0–2). While this does not affect the measurement of  $b_\phi$ , it is critical for the error bars. However, we have no guarantee that this relation of  $\rho$  with the mass would saturate at some point. Therefore, we have chosen a more conservative approach (as it results in larger reported uncertainties) and assume for the bins 0–2 the average  $\rho$  that we have calculated from the FASTPM mocks (i.e. bins 3–10), giving for those bins  $\rho = 0.703$ .

In addition, we propose to apply this to constrain directly the product  $b_\phi f_{\text{NL}}$  (instead of just  $f_{\text{NL}}$  as done in Avila & Adame (2023)), which is the quantity we are sensitive to. To this end, we construct this new estimator for  $b_\phi f_{\text{NL}}$ , which takes into account the matching between both simulations:

$$\Delta b_\phi f_{\text{NL}} = [b_\phi f_{\text{NL}}]_{100} - [b_\phi f_{\text{NL}}]_0, \quad (16)$$

where  $[b_\phi f_{\text{NL}}]_{100}$  is the quantity measured in the non-Gaussian simulation with  $f_{\text{NL}} = 100$  and  $[b_\phi f_{\text{NL}}]_0$  corresponds to the Gaussian one. Given that the noise in  $[b_\phi f_{\text{NL}}]_{100}$  and  $[b_\phi f_{\text{NL}}]_0$  is highly correlated, it is expected that the average  $\Delta b_\phi f_{\text{NL}}$  would converge to the mean much faster than the average of  $[b_\phi f_{\text{NL}}]_{100}$  or  $[b_\phi f_{\text{NL}}]_0$  alone, since we are cancelling some part of the noise. The variance of  $\Delta b_\phi f_{\text{NL}}$  is given by

$$\sigma^2(\Delta b_\phi f_{\text{NL}}) = \sigma^2([b_\phi f_{\text{NL}}]_{100}) + \sigma^2([b_\phi f_{\text{NL}}]_0) - 2\rho\sigma([b_\phi f_{\text{NL}}]_{100})\sigma([b_\phi f_{\text{NL}}]_0), \quad (17)$$

where  $\sigma([b_\phi f_{\text{NL}}]_{100})$  is the error of the quantity measured in the non-Gaussian simulation and  $\sigma([b_\phi f_{\text{NL}}]_0)$  corresponds to the Gaussian one, and  $\rho$  is the correlation coefficient between the two measured using the FASTPM mocks.

While, in principle, this method can be applied to any two values of  $f_{\text{NL}}$ , the advantage of choosing one value to be  $f_{\text{NL}} = 0$  is that  $\langle \Delta b_\phi f_{\text{NL}} \rangle = \langle [b_\phi f_{\text{NL}}]_{100} \rangle$ . From now on, when we apply this matching, we label the errors as  $\sigma_{S+M}$  if we use Equation 14 for the variance of the power spectrum and  $\sigma_{F+M}$  if we use the method described in Section 4.2.

#### 4.4. Variance estimation methods

In the previous sections, we discuss how to reduce the noise in the measurements of  $b_\phi f_{\text{NL}}$  by taking advantage of the fixed-and-matched initial conditions of the PNG-UNIT. We compare our results with those derived when no noise reduction techniques are employed to ensure that we are not introducing any bias when using these techniques.

We defined the following errors for the power spectrum,  $\sigma(P(k))$ :

- Standard errors,  $\sigma_S$ , come from Equation 14 with only one simulation used to measure  $b_\phi f_{\text{NL}}$ . This error is not correlated with the other  $f_{\text{NL}}$  simulation. This method is expected to provide the largest estimate of the error.
- Fixed errors,  $\sigma_F$ , are obtained from the best-fit  $\sigma(P(k))$  (Equation 15) measured from the FASTPM mocks for bins 3–10 in halo mass. For bins 0–2 and 10–12, we do not recover the clustering nor the abundances with FASTPM mocks simultaneously, so we need to perform an extrapolation for those mass bins (Section 4.3). To obtain these errors, we do not correlate  $f_{\text{NL}} = 0$  with  $f_{\text{NL}} = 100$ .

In addition, we have errors that take into account the noise reduction due to the fixed-and-matched initial conditions (Equation 17):

- ‘standard + matched’ error,  $\sigma_{S+M}$ , where the standard error  $\sigma_S$  for the power spectrum from the simulations with  $f_{\text{NL}} = 0$  is correlated with the ones with  $f_{\text{NL}} = 100$  using the method described in Section 4.3;
- ‘fixed + matched’ errors,  $\sigma_{F+M}$ , where we assume the  $\sigma_F$  errors for the power spectrum and correlate matched simulations with different  $f_{\text{NL}}$ . We consider these errors for the baseline analysis.

In Section 7.2, we compare how these assumptions affect the constraints on  $b_\phi$  and  $p$ .

## 5. Constraining the PNG bias parameters for mass-selected halos

Given the input value of  $f_{\text{NL}}$  used to generate the initial conditions for the PNG-UNIT, we can measure directly  $b_\phi$  from the scale-dependent bias (Equation 11). In this section, we discuss how we constrain  $b_\phi$  for mass-selected halos using the suppressed variance from the matching technique (§4.3).

First, we check how well Equation 11 describes the clustering of the dark matter halos in the PNG-UNIT under the standard assumption that  $b_\phi$  is given by the universality relation (i.e.  $p = 1$ ). We measure the non-Gaussian signal  $b_\phi f_{\text{NL}}$  in our simulations (§5.2), and by assuming the universality relation, we report our results for  $f_{\text{NL}}$  (§5.3). Finally, using the input values of  $f_{\text{NL}}$ , we directly measure  $p$  (§5.4). In Table 3, we summarise the main results from this section.

### 5.1. Parameter estimation and analysis choices

Here, we describe the pipeline applied for parameter estimation common to all our analyses. We study the impact of varying these assumptions in Section 7.

To obtain the PNG parameters, we performed Markov chain Monte Carlo (MCMC) using the Python package `EMCEE`<sup>9</sup> (Foreman-Mackey et al. 2013). All the cosmological parameters are fixed except  $b_1$  and  $b_\phi f_{\text{NL}}$  for which we set flat priors over a wide range ( $[0, 10]$  for  $b_1$  and  $[-10000, 10000]$  for  $b_\phi f_{\text{NL}}$ ). We assume a Gaussian likelihood with  $\chi^2$  given by

$$\chi^2 = \sum_{i=0}^{N_k} \frac{(P_{\text{halos}}(k_i) - P_{\text{model}}(k_i; b_1; b_\phi f_{\text{NL}}))^2}{\sigma^2(P(k_i))}. \quad (18)$$

Here,  $P_{\text{model}}(k)$  is obtained using Equation 11 by inputting the matter power spectrum  $P_{m,m}(k)$  computed directly from the simulation. In the baseline analysis, we use the fixed+matched errors  $\sigma_{F+M}$  defined in Section 4.4 for  $\sigma(P(k))$ . Moreover, in the subsequent figures, we use solid circles when we are using the best fit to Equation 15 and the mocks, and we use empty circles when we performed extrapolation (i.e. for bins 0-2). We then obtain  $\sigma(b_\phi f_{\text{NL}})$  from the posterior distribution after marginalising over  $b_1$ . The model described by Equation 11 is only accurate in the purely linear regime.

Due to the limitation of our model to the linear regime, we need to drop the modes associated with higher-order nonlinear terms in the power spectrum and consider only the linear modes by applying a scale cut. We choose to set  $k_{\text{max}} = 0.1 \text{ h Mpc}^{-1}$ , as the next-to-leading order terms become important beyond this scale. In Section 7, we discuss this issue and study its impact on the  $b_\phi$  and  $f_{\text{NL}}$  constraints, where we find that variations of 50% in  $k_{\text{max}}$  compared to our fiducial choice have a negligible effect.

<sup>9</sup> <https://emcee.readthedocs.io/en/stable/>

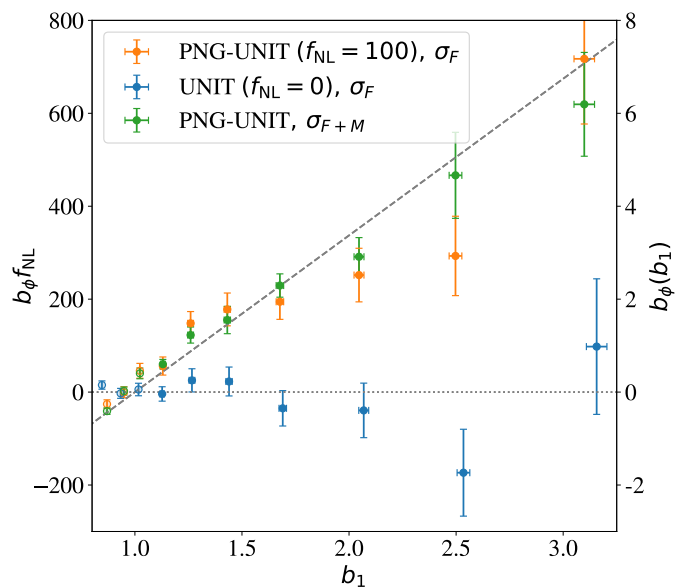


**Fig. 5.** Constraints on  $b_\phi f_{\text{NL}}$  as a function of  $b_1$ . Blue and orange symbols show results for the Gaussian and the non-Gaussian simulations, respectively, assuming that the  $P(k)$  variance is computed from the FASTPM mocks (see §4.2). By subtracting both, we obtain the green points. Thanks to the so-called matching technique, these points have smaller uncertainties (see Equation 16 and Equation 17 in §4.3). Grey lines indicate the expected value by assuming the universality relation, with the dotted line for  $f_{\text{NL}} = 0$  and the dashed line for  $f_{\text{NL}} = 100$ . In solid circles, we use the best fit to Equation 15 for estimating the power spectrum variance; in rings, we use the extrapolation method. Here, mass bins 0-9 are shown.

### 5.2. Constraints on $b_\phi f_{\text{NL}}$

Following the pipeline described above, we fix all the cosmological parameters for our analysis, except  $b_1$  and  $b_\phi f_{\text{NL}}$  in Equation 11, and then search for the best-fit parameters.

We show the results in the third column of Table 3 and in Figure 5, where the blue and orange symbols represent the best-fit values for the Gaussian and non-Gaussian simulations, respectively, and the dashed and dotted lines indicate the expected values for each case. The error bars show the 68% confidence interval obtained from our fits for  $b_\phi f_{\text{NL}}$ . For the blue and orange data points, we have used the variances obtained from the fits to the FASTPM mocks (see §4.2), while for the green symbols, we have used the fixed-and-matched technique (see §4.3). We expected to obtain exactly zero for the Gaussian simulation, while for the non-Gaussian one, the reference we compare to is the universality relation prediction (i.e.  $p = 1$ ). The grey lines show these expectations. For halos with  $b_1 > 1$ , we clearly measure  $b_\phi f_{\text{NL}}$ . When  $b_1 \sim 1$ , for the most popular assumption of  $p = 1$  in Equation 13,  $b_\phi$  is nearly zero and the non-Gaussian signal is masked. In the same figure, we also observe fluctuations for the  $f_{\text{NL}} = 0$  simulation around zero, which is expected due to the intrinsic cosmic variance of the simulation.

Since both simulations originate from the same random phases, we expect the measurements of  $b_\phi f_{\text{NL}}$  to be highly correlated (§4.3). Therefore, if we find perturbation in the Gaussian simulation ( $f_{\text{NL}} = 0$ ) that lowers the measured  $b_\phi f_{\text{NL}}$ , an equivalent perturbation is expected to appear in the non-Gaussian ( $f_{\text{NL}} = 100$ ) simulation, as we see in Figure 5 indeed.

We apply Equations 16 and 17 to compute the matched data points from both simulations, obtaining the green points in Fig-

ure 5. We expect that these results have less noise than the individual cases of the simulations because of the correlations in the initial conditions. We find the green points to be closer to the prediction from the universality relation ( $p = 1$ ). While this is true for  $M_{\text{halo}} > 1 \times 10^{12} h^{-1} M_{\odot}$ , we find that the measured  $p$  is below that of the universality relation for masses with  $M_{\text{halo}} < 1 \times 10^{12} h^{-1} M_{\odot}$ , with a significance that reaches  $3\sigma$  for bin 2.

Regarding the mass range from  $M_{\text{halo}} = 5 \times 10^{13} h^{-1} M_{\odot}$  up to  $5 \times 10^{14} h^{-1} M_{\odot}$  (bins 10-12 in Table 3, not shown from Figure 5 on), their power spectra exhibit a very low signal-to-noise ratio ( $S/N < 5$ ) due to their low number densities ( $n_{\text{halos}} \ll 10^{-4} h^3 \text{Mpc}^{-3}$ ). As we discussed in Section 4.2, to estimate the covariance for the power spectra, we considered two cases: applying Equation 14 or the extrapolation of Equation 15. When considering  $\sigma_S(P(k))$ , a more detailed analysis of these bins reveals that considering a super-Poisson contribution to the shotnoise ( $\propto (1 + \alpha)/n_g$ ) is necessary to have an accurate estimation of the variance of the power spectrum,  $\sigma(P(k))$ . At the same time, this extra noise, parameterised by  $\alpha$ , is consistent with  $\alpha = 0$  for the rest of the bins (0–9), which is our assumed baseline. We leave for future analysis the usage of non-Poisson errors as our analysis baseline. Thus, in what follows, we only analyse halos with masses  $2 \times 10^{10} < M_{\text{halo}}(h^{-1} M_{\odot}) \leq 5 \times 10^{13}$ , which correspond to bins 0 to 9 in Table 3.

### 5.3. Measuring $f_{\text{NL}}$ from $b_{\phi} f_{\text{NL}}$ assuming the universality relation

We cannot constrain both  $b_{\phi}$  and  $f_{\text{NL}}$  simultaneously since they are perfectly degenerate. We can do so, however, by assuming the universality relation with  $p = 1$ . In this way, we extract  $f_{\text{NL}}$  from our simulation results. If this relation does not accurately describe the  $b_{\phi}$  parameter, we expect to recover biased values of  $f_{\text{NL}}$ . Hence, we have tested the validity of the universality relation.

In Figure 6, we compare the values of  $f_{\text{NL}}$  obtained in this way with the ones set in the initial conditions. We find that the perturbations that favour a positive value of  $f_{\text{NL}}$  in the Gaussian simulation are also present in the non-Gaussian one. The results are shown in blue symbols for the  $f_{\text{NL}} = 0$  simulation and orange symbols for the  $f_{\text{NL}} = 100$  simulation. We reduce the noise in  $f_{\text{NL}}$  by applying the matching technique. This involves the estimation of  $b_{\phi} f_{\text{NL}}$  using Equation 16 and its variance through Equation 17. In the Gaussian simulation, the expected value for  $b_{\phi} f_{\text{NL}}$  is 0. This means that the expected value of  $\Delta b_{\phi} f_{\text{NL}}$  is the same as the  $b_{\phi} f_{\text{NL}}$  of the simulation with  $f_{\text{NL}} = 100$ . Then, we divide by  $b_{\phi}$  computed assuming  $p = 1$ . Using this correlation, we determine the combined measurement of  $f_{\text{NL}}$ , shown in green symbols in Figure 6.

For masses between  $5 \times 10^{10}$  and  $2 \times 10^{11} h^{-1} M_{\odot}$ , the error bars are enlarged because  $b_1 \sim 1$  for those bins, so using the universality relation results in  $b_{\phi} \sim 0$ . Moreover, a slight deviation from the expected value in  $b_{\phi} f_{\text{NL}}$  assuming universality in these mass bins leads to an amplification of this deviation from the input value in  $f_{\text{NL}}$ , precisely because  $b_{\phi}$  is close to 0. This is what we observe for bins 2 and 3. Nevertheless, considering also the growth of the errorbars, for halos with masses between  $M_{\text{halo}} = 1 \times 10^{11} h^{-1} M_{\odot}$  and  $M_{\text{halo}} = 1 \times 10^{12} h^{-1} M_{\odot}$  we find deviations from the input value, with a significance up to  $4\sigma$  in the case of bin 2. These differences, which we have already seen in  $b_{\phi} f_{\text{NL}}$  in Figure 5, can be interpreted as meaning that the population of halos in that mass bin have  $b_{\phi}$  that does not follow the universality relation, as we assumed  $p = 1$  for deriving these

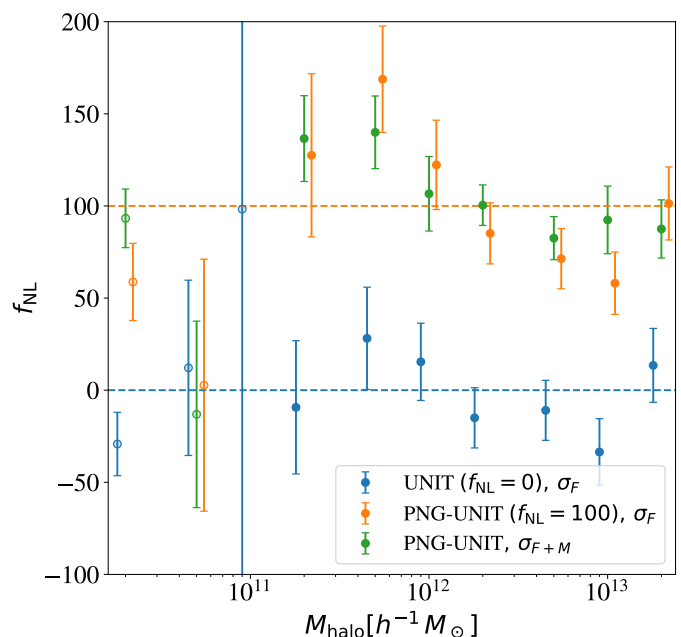


Fig. 6. Value of  $f_{\text{NL}}$  for each mass bin, assuming  $b_{\phi}$  is described by Equation 13 with  $p = 1$ . Blue and orange symbols show results for the Gaussian and non-Gaussian simulations, respectively. In contrast, green symbols show the matching (difference) between them, where we used Equation 16 for obtaining  $b_{\phi} f_{\text{NL}}$  and Equation 17 for its uncertainty. Dashed lines show the input  $f_{\text{NL}}$  values for each simulation. For the mass bins 2 and 3, we have that  $b_1 - 1 \leq 0.1$  and hence  $b_{\phi} \sim 0$ . This value of  $b_{\phi}$  explains the large error bars compared to the other mass bins. In solid circles, we use the best fit to Equation 15 for estimating the power spectrum variance; in rings, we use the extrapolation method.

measurements of  $f_{\text{NL}}$ . Finally, we recover the input value of  $f_{\text{NL}}$  for both simulations for halos with  $M_{\text{halo}} > 1 \times 10^{12} h^{-1} M_{\odot}$  (see Table 3).

### 5.4. $p$ as a function of mass

Since we know the input value of  $f_{\text{NL}}$ , we can use the deviations of our measurements from that value to find how far the assumption  $p = 1$  is from the  $p$  measured for the simulation halos.

We fix the value of  $f_{\text{NL}}$  and derive  $b_{\phi}$  from the previous constraints on  $b_{\phi} f_{\text{NL}}$  we obtained in Section 5.2. We then compute  $p$  using Equation 13. We have also checked that we get the same results by fitting  $p$  directly and fixing  $f_{\text{NL}}$  to its input value in a similar way as done in Section 5.3.

The results are shown in Figure 7, where we compare the different methods of estimating the variance of the power spectrum and reducing the noise introduced in Section 4.4. Our methodology is consistent as we recover the same results regardless of the method used for estimating the variance of the power spectrum with or without the matching technique. The clustering of the halos with  $1 \times 10^{12} < M_{\text{halo}} < 2 \times 10^{13} h^{-1} M_{\odot}$  are aptly described through the universality relation ( $p = 1$ ), given the size of our uncertainties. Concerning the mass bins with  $M_{\text{halo}} < 5 \times 10^{11}$ , we find a slight deviation from  $p = 1$ , with a significance that reach  $> 3\sigma$  for halos with masses between  $1 \times 10^{11}$  and  $2 \times 10^{11} h^{-1} M_{\odot}$ . These lower values of  $p$  are related to the overprediction of the product  $b_{\phi} f_{\text{NL}}$  (§5.2).

We explore the possibility of  $p$  being a constant independent of the halo mass. We do this by performing a linear fit. We obtain

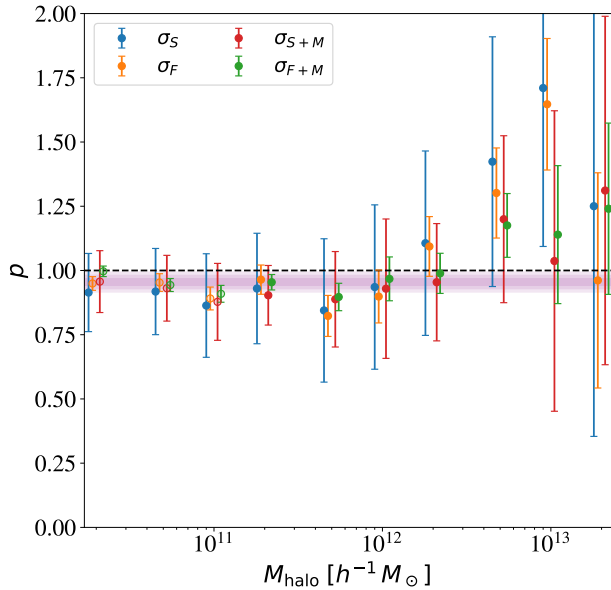


**Fig. 7.** PNG-response parameter  $p$  as a function of the halo mass, using different methods to treat variances. Blue and orange symbols show results for the non-Gaussian simulation, using standard variances (Equation 14) and fixed variances, respectively. Green and red symbols show the same after applying the matching with the Gaussian simulation. In solid circles, the fixed variances is estimated by the best fit to the FASTPM variances with Equation 15; in rings, we use the extrapolation method. The shaded areas represent the  $1\sigma$ ,  $2\sigma$  and the  $3\sigma$  regions (from darker to lighter respectively) around the value of  $p$  we find in Equation 19.

a slope consistent with zero at  $1\sigma$ , suggesting that a constant  $p$  can indeed be assumed for the halos. By an average weighted by the inverse of the variance, we get:

$$p = 0.955 \pm 0.013 \quad (19)$$

with  $\chi^2/\text{dof} = 1.31$  when we take into account all the bins (0–9), while the  $\chi^2/\text{dof}$  for  $p = 1$  is 2.64. This best-fit value of  $p$  with the  $1, 2$  and  $3\sigma$  regions are shown as the shaded region in Figure 7. If we neglect those bins where we used extrapolation (i.e. by removing the mass bins 0-2 from the fits and considering just 3-9), we get:

$$p = 0.950 \pm 0.025 \quad (20)$$

with a  $\chi^2/\text{dof}$  of 1.33.

## 6. Convergence tests

This section shows how far we can push our results to low masses. To do so, we test the convergence of the PNG-UNIT against the LR-UNIT simulations with a lower resolution (§6.1). We also demonstrate the robustness of our results by comparing them with an alternative method to measure  $b_\phi$ , using the separate universe approach (§6.2). Finally, we investigate the impact of considering different mass definitions (§6.3).

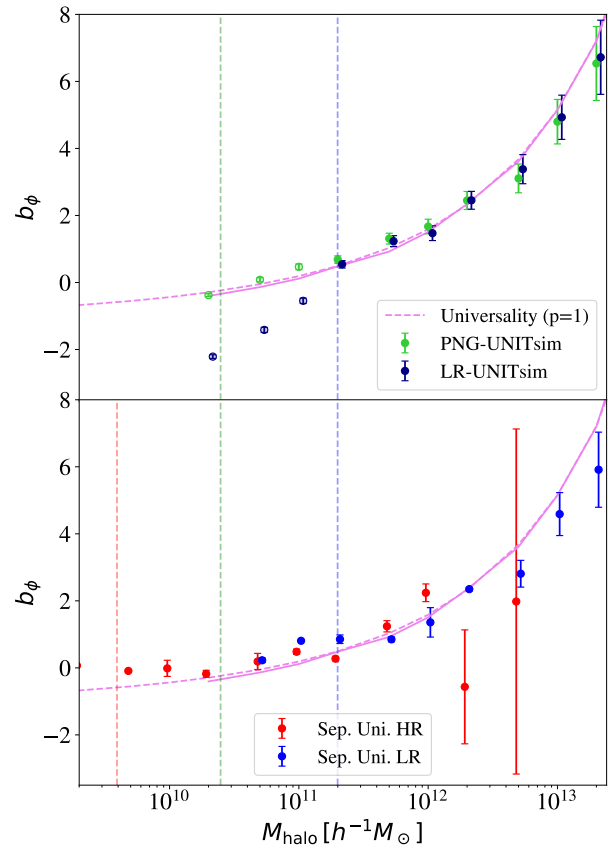


**Fig. 8.** Non-Gaussian bias parameter  $b_\phi$  as a function of the halo mass for the different sets of simulations. The colour of the symbols and the dashed lines represent the mass resolution. Red:  $m_p = 1.5 \times 10^8 [h^{-1} M_\odot]$ . Green:  $m_p = 1.2 \times 10^9 [h^{-1} M_\odot]$ . Blue-Dark blue:  $m_p = 1.0 \times 10^{10} [h^{-1} M_\odot]$ . The dashed vertical lines represent the threshold of  $M_{\text{halo}} = 20m_{\text{part}}$  for each simulation. The pink solid line is the universality relation  $p = 1$  for the  $b_1$  values measured in the PNG-UNIT. The dashed pink line extrapolates the universality relation toward lower masses, using  $b_1$  coming from Tinker et al. (2010). In solid circles, we use the best fit to Equation 15 for estimating the power spectrum variance; in rings, we use the extrapolation method. Upper panel: Measurements of  $b_\phi$  in non-Gaussian simulations by fitting Equation 11 (see §6.1). Lower panel: Measurements of  $b_\phi$  using the separate universe technique (see §6.2).

### 6.1. Convergence with LR-UNIT simulations

First, we investigate the mass convergence of our results by comparing the PNG-UNIT results with those of the lower-resolution LR-UNIT simulations. Our methodology is the same as in Section 5.2, and we assume  $\sigma_{F+M}$  errors.

The upper panel of Figure 8 compares the values of  $b_\phi$  derived from the  $4096^3$ -particle simulations with those from the LR-UNIT simulations. The  $b_\phi$  values agree for bins with  $M_{\text{halo}} \geq 20m_{\text{part,LR}}$ . Below this threshold, the mass function from the LR-UNIT simulations drops as we cannot resolve such light halos (Figure 2). This drop in the abundance of halos also affects the clustering, as demonstrated by the sudden change in  $b_\phi$ . Thus,

we prove that the limit of 20 particles is an adequate minimum threshold for the halo mass considered for our simulations.

The universality relation ( $p = 1$ ) is shown as a solid pink line in Figure 8, assuming the  $b_1$  values from the fits of the PNG-UNIT to the corresponding mass resolution. To extend the relation beyond the mass resolution of the N-body simulations, we have also used the theoretical values for  $b_1(M)$  derived using Tinker et al. (2010) for each bin in halo mass, given the simulation cosmology. This extrapolation is shown as dashed pink lines in the upper panel of Figure 8. These two lines are consistent with each other.

The derived  $b_\phi$  values agree in both resolutions for halos with more than 20 particles. Although not shown here, we have checked that the results from running LR-UNIT with 2LPTc (Crocco et al. 2006, 2012) initial conditions are consistent with those from LR-UNIT initialised with FASTPM. In a forthcoming paper, we study the impact of using different codes for the initial conditions in simulations with primordial non-Gaussianities.

Finally, we measure  $p$  from the LR-UNIT simulations by fixing  $b_1$  to Tinker et al. (2010) in Equation 13. We obtain similar results for  $p$  using  $b_1$  directly obtained from the simulations. Combining all the mass bins with  $M_{\text{halo}} > 20m_{\text{part}}$ , we obtain  $p = 0.959 \pm 0.014$  for the PNG-UNIT and  $p = 0.972 \pm 0.017$  for the LR-UNIT. These values are consistent with Equation 19.

## 6.2. Comparison with separate universe simulations

As a further test of the robustness of our results, we compare two alternative methods for measuring  $b_\phi$ : (i) using the scale-dependent bias as we have done throughout this paper and (ii) using the so-called separate universe technique. This latter technique exploits the fact that  $b_\phi$  is defined as the response of the abundance of halos to the presence of a large-scale perturbation (Equation 12).

The separate universe technique consists of computing  $b_\phi$  as the numerical derivative of two simulations with the same initial conditions but with a slightly different  $\mathcal{A}_s$ , or equivalently,  $\sigma_8$ . The initial conditions for these simulations are Gaussian; thus, these simulations do not show the effect of the scale-dependent bias. Following a similar procedure as done in Barreira et al. (2020); Barreira (2022c),  $b_\phi$  is obtained as follows:

$$b_\phi = \frac{b_\phi^{\text{high}} + b_\phi^{\text{low}}}{2}, \quad (21)$$

with

$$b_\phi^{\text{high}} = \frac{4}{\delta\mathcal{A}_s N_h^{\text{fid}}} (N_h^{\text{high}} - N_h^{\text{fid}}), \quad (22)$$

$$b_\phi^{\text{low}} = \frac{4}{\delta\mathcal{A}_s N_h^{\text{fid}}} (N_h^{\text{fid}} - N_h^{\text{low}}).$$

In Equation 22,  $\delta\mathcal{A}_s$  is the variation in the amplitude of the initial power spectrum (which we set to 5%), and  $N_h$  is the number of halos within a particular mass bin measured in the simulations. For the separate universe technique, we estimate the error in  $b_\phi$ ,  $\sigma_{\text{SU}}(b_\phi)$ , following the same consideration as Barreira et al. (2020) and Barreira (2022c):

$$\sigma_{\text{SU}}(b_\phi) \sim |b_\phi^{\text{high}} - b_\phi^{\text{low}}|. \quad (23)$$

The lower panel of Figure 8 compares the  $b_\phi$  values obtained from using the separate universe technique (Equation 22) for two sets of simulations with different mass resolutions. Comparing

this method for measuring  $b_\phi$  with respect to the one we have been considering in Section 5.2 is a way to check the consistency across the two different methods and whether they hold at low masses.

The universality relation is displayed as pink lines in Figure 8. We used both the linear bias,  $b_1$ , coming from the measurements on the PNG-UNIT simulation (continuous line) and  $b_1$  coming from Tinker et al. (2010) (dashed line). We do not measure  $b_1$  from the separate universe simulations as the box size of the simulations is relatively small ( $L_{\text{box}} = 67.5 h^{-1} \text{Mpc}$  and  $L_{\text{box}} = 250 h^{-1} \text{Mpc}$  for the high-resolution and low-resolution simulations respectively) and direct measurement of the linear bias through the halo power spectrum may be significantly contaminated by the non-linearities of the small scales ( $k_{f,\text{HR}} \sim 0.09 h \text{Mpc}^{-1}$  and  $k_{f,\text{LR}} \sim 0.02 h \text{Mpc}^{-1}$ ).

The error bars obtained for the separate universe method might not be robust. On the one hand, we find that the high-resolution separate universe simulations do not agree with the low-resolution simulations, as shown in the lower panel of Figure 8. The real error bars should, at least, reflect the difference between both. On the other hand, the scatter around the universality relation is much bigger than the error bar reported by this method. This is specially significant for  $M_{\text{halo}}$  between  $1 \times 10^{11} h^{-1} M_\odot$  and  $5 \times 10^{11} h^{-1} M_\odot$ .

We estimate a global error in  $b_\phi$  by combining the measurements from both the high and low-resolution simulations, taking the mean value and the absolute difference as the error, similar to what we did to compute  $b_\phi$  from the high-As and the low-As simulations in Equation 21 and Equation 23. With this procedure, we expect to obtain more reliable errors than those from a single set of simulations (i.e. high or low-resolution).

Finally, we measure  $p$  from the separate universe. We fit  $b_\phi$  to Equation 13 using a least-squares method, with  $b_1$  coming from Tinker et al. (2010) for each mass bin. Utilising the error in  $b_\phi$  for the combination of the high- and low-resolution separate universe simulations we have described, we get  $p = 0.8307 \pm 0.0022$ . This result differs from the universality relation and the  $p$  obtained for the PNG-UNIT, Equation 19. We argue that this suggests a shortcoming in the method used to obtain  $\sigma_{\text{SU}}(b_\phi)$ . The mass bins with the smallest errors drive the separate universe measurement of  $p$ . Moreover,  $\chi^2/\text{dof} = 519/20$  for the  $p$  obtained with the separate universe technique is rather large.

Ignoring the separate universe error bars, we find  $p = 1.047 \pm 0.057$  by not weighting the bins by their  $\sigma(b_\phi)$  in the least-squares fitting procedure. If we apply this method to the results coming from PNG-UNIT simulation, we get  $p = 0.984 \pm 0.031$ . In both cases, the value is consistent with the universality relation, and it is less than  $2\sigma$  away from the results shown in Equation 19.

Overall, the results in this section suggest that one must be very careful when considering the errors in  $b_\phi$  arising from the separate universe technique and consider a larger set of simulations to deal with them statistically. Given the setup considered in this paper, the error bars reported are more robust for PNG-UNITsims, and the underlying true uncertainty seems smaller for PNG-UNITsims.

## 6.3. Dependency on the mass definition

If  $b_\phi$  depends on the halo mass only by its dependence on  $b_1$ , then the relationship between these two quantities should be independent of the mass definition used for halos.

Throughout this work, the halo masses have been obtained by computing the enclosed mass within a spherical overdensity up to 200 times the critical density  $\rho_c$  at a given  $z$ ,  $M_{200c}$ . Here, we redo the analysis to obtain  $p$  using other mass definitions, namely:  $M_{500c}$ ,  $M_{200b}$  and  $M_{\text{vir}}$ . The radii used for these mass definitions are determined by the threshold density achieved within the spherical overdensity, which reaches 500 the critical density  $\rho_c$  for  $M_{500c}$  and 200 times the background density  $\rho_b$  for  $M_{200b}$ . For the virial mass  $M_{\text{vir}}$ , the spherical overdensity is determined by the virial radius  $r_{\text{vir}}$  (Bryan & Norman 1998).

We have  $M_{200c} \geq M_{500c}$  for a given halo. Thus, if we apply the same mass cuts for defining the bin, we expect that  $b_1(M_{200c}) < b_1(M_{500c})$ , as if we compare the  $M_{200c}$  of the halos selected in each case, we are taking more massive halos when we apply the cut in  $M_{500c}$ . However, although we expect that  $b_\phi(M_{200c}) \neq b_\phi(M_{500c})$  if  $b_\phi$  only depends on the mass through  $b_1$ , we would expect that  $p$  does not vary with the mass definition.

We present our findings in Figure 9 which compares four mass definitions outputted by ROCKSTAR: our fiducial  $M_{200c}$ ,  $M_{500c}$ ,  $M_{200b}$  and  $M_{\text{vir}}$ . There are several things to point out. We find that bins defined according to  $M_{200b}$  and  $M_{\text{vir}}$  are practically equal between them and very similar to  $M_{200c}$ . Moreover, they have almost the same  $b_1$ , although this is not shown here. For these three cases, the results are consistent with our findings in Section 5.4.

However, the most interesting result comes from the bins defined according to  $M_{500c}$ . We find a systematic suppression of  $p$  below the predicted value from the universality relation and compared with the other mass definitions, although the error bars cover  $p = 1$ . This result suggests that  $b_\phi$  for dark matter halos may not depend solely on the mass through  $b_1$  but also on other parameters. The  $b_\phi$  parameter is defined as how the abundance of the dark-matter halos responds to a large-scale perturbation. However, PNG may not only affect the amplitude of the primordial perturbations (and hence the abundance of the high-mass halos) but also could affect other properties of the halo as suggested by recent works (Sullivan et al. 2023; Lazeyras et al. 2023; Lucie-Smith et al. 2023; Fondi et al. 2024). Investigating this dependence is beyond the scope of this paper and is left for future research.

We also tested the impact on  $b_\phi$  if we consider the main halos and the subhalos identified by ROCKSTAR. This consideration might be necessary if one runs subhalo abundance matching (SHAM) algorithms to populate the simulation with galaxies. When the substructure is included in the analysis, we find that this induces variations in the linear bias  $b_1$  of the mass bins and in  $p$ . We leave a detailed analysis of this for future work.

## 7. Robustness tests

Here, we test the impact of the assumptions we have made in our analysis to obtain  $b_\phi$  or  $p$ . In particular, we study the impact of the scale cut,  $k_{\text{max}}$  (§7.1), and the variance estimation methods described in Section 4.4.

### 7.1. Choice of $k_{\text{max}}$

Equation 11 is only valid in the linear regime, thus, we must discard all modes with  $k$  greater than a certain  $k_{\text{max}}$  to avoid introducing non-linear modes our model does not properly describe. As perturbation theory breaks beyond  $k_{\text{NL}} \sim 0.3 \text{ h Mpc}^{-1}$  (Desjacques et al. 2018),  $k_{\text{max}}$  should be less than this value. Even

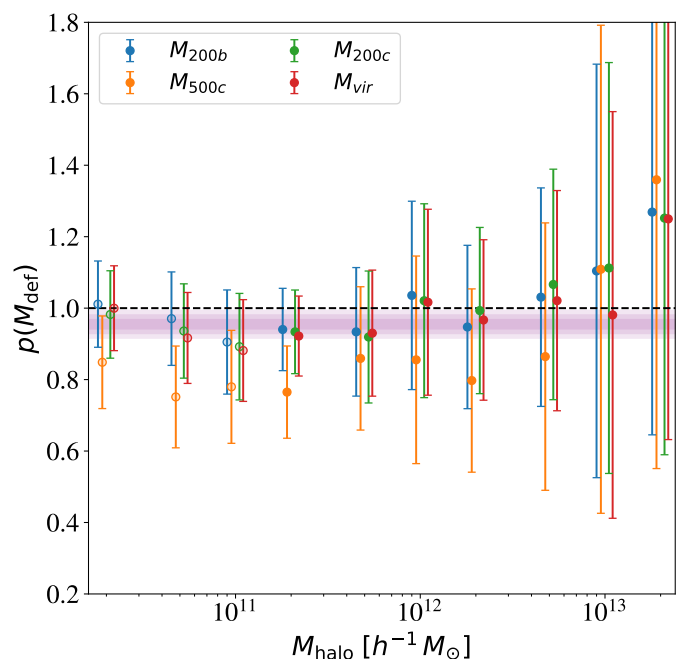


**Fig. 9.** PNG bias parameter  $p$  as a function of  $M_{\text{halo}}$  for different mass definitions. The green symbols represent our choice for the fiducial analysis ( $M_{200c}$ ), while the grey dashed line represents the universality relation ( $p = 1$ ). The shaded areas represent the  $1\sigma$ ,  $2\sigma$  and  $3\sigma$  regions (from darker to lighter respectively) around the value of  $p$  we find in Equation 19. Masses are shifted for visualisation purposes.

before reaching this threshold, we are at the risk of incorporating some mildly non-linear modes that our model does not adequately describe.

To determine the optimal  $k_{\text{max}}$ , we must first examine the limits of the linear theory using only the Gaussian simulation. In this case, Equation 11 is reduced to  $P_{h,h}(k) = b_1^2 P_{m,m}(k)$ . The leading correction of the non-linear bias to  $P_{h,h}(k)$  has a dependence with  $Ak^2$ , where  $A$  is a nuisance parameter (Lazeyras & Schmidt 2018; Lazeyras et al. 2023). To establish  $k_{\text{max}}$ , we compare the fits obtained using only  $b_1$  with those obtained using  $b_1 + Ak^2$  after marginalising over the nuisance parameter  $A$  as a function of  $k_{\text{max}}$ . We find that the differences in the posterior distributions for  $b_1$  obtained using both methods agree for  $k_{\text{max}} \leq 0.1 \text{ h Mpc}^{-1}$  for all mass bins.

We proceed similarly with the non-Gaussian simulation. Starting from our fiducial choice of  $k_{\text{max}} = 0.1 \text{ h Mpc}^{-1}$ , we test both the lower and higher values. Our results show that varying the  $k_{\text{max}}$  has a minimal impact on  $p$ , with all central values remaining within  $1\sigma$  when  $k_{\text{max}}$  is varied from  $0.07$  to  $0.15 \text{ h Mpc}^{-1}$ . This is shown in panel (a) of Figure 10. The error bars shrink by approximately  $\sim 20\%$  throughout this range when considering a larger  $k_{\text{max}}$ . Furthermore, we performed a linear fit for  $p$  as a function of mass (as described in Section 5.4) and we find that the slope is consistent with zero. If we compute the weighted average of bins 0–9, we find that  $p(k_{\text{max}} = 0.07 \text{ h Mpc}^{-1}) = 0.933 \pm 0.013$  and  $p(k_{\text{max}} = 0.15 \text{ h Mpc}^{-1}) = 0.947 \pm 0.012$ , in agreement with our previous findings for our fiducial choice of  $k_{\text{max}}$ .

Going beyond the purely linear modes may bias the constraints on  $b_1$  (since those modes are not properly modelled) and hence the constraints on  $b_\phi$  and  $p$ . We therefore set the cutoff at  $k_{\text{max}} = 0.1 \text{ h Mpc}^{-1}$ . On the one hand, we have shown that the

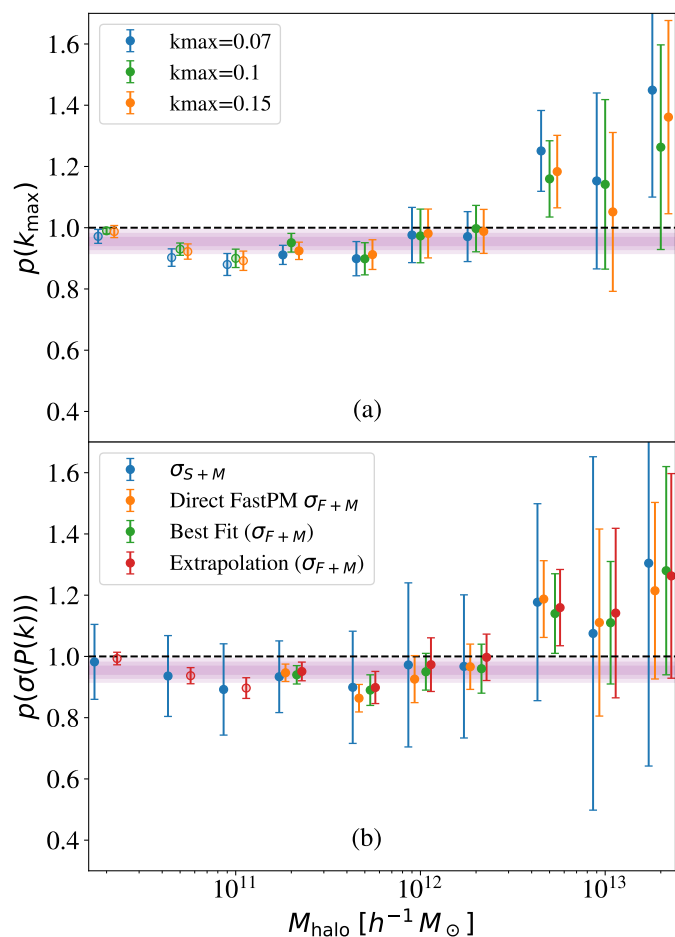


**Fig. 10.** PNG bias parameter  $p$  as a function of  $M_{\text{halo}}$  for different analysis choices. The green symbols represent the fiducial choices, while the grey dashed line represents the universality relation ( $p = 1$ ). In solid circles, we use the best fit to Equation 15 for estimating the power spectrum variance; in rings, we use the extrapolation method. The shaded areas represent the  $1\sigma$ ,  $2\sigma$  and the  $3\sigma$  regions (from darker to lighter respectively) around the value of  $p$  we find in Equation 19. Masses are shifted for visualisation purposes. Panel (a): variation in  $p$  with changes  $k_{\text{max}}$  (see §7.1). Panel (b): constraints on  $p$  by considering different methods to compute  $\sigma(P(k))$ , namely: standard  $\sigma_S(P(k))$  (blue), direct fit to FASTPM mocks (orange), best-fit to Equation 15 (green) and extrapolation of Equation 15 to the mass bins (red) (see §7.2).

results are consistent even if this value is varied by  $\sim 50\%$ . On the other hand, this is a standard choice, and it is more conservative than continuing to push to higher  $k$ , where we might have to deal with non-linear terms.

## 7.2. Power spectrum variance from FASTPM

An accurate estimation of the variance of the halo power spectrum,  $\sigma(P(k))$ , is critical when we perform parameter estimation, given that this quantity enters the computation of the likelihood. However, we know that the standard approach of Equation 14 overestimates the variance of our simulations as they have fixed initial conditions. In Section 4.2, we discuss how we estimated  $\sigma(P(k))$  from the FASTPM mocks, which take into account the effect of the fixed ICs. We show how, by fitting  $\sigma(P(k))/P(k)$  to Equation 15, we can even extrapolate to masses where we are

not able to generate the ‘equivalent’ mass bins to the ones from the N-body simulation.

Here, we check the impact of considering different ways of computing the power spectrum variance on  $p$ . In particular, we consider the four different methods (see §4.2). First of all we consider the standard variances,  $\sigma_S(P(k))$ , computed from Equation 14 (blue symbols in panel (b) of Figure 10). Then we consider the direct FASTPM variances,  $\sigma_{F+M}(P(k))$ , obtained by computing directly the standard deviation of the power spectrum of the fast simulations (orange symbols). We also consider the best-fit of FASTPM variances using Equation 15 (green symbols). And finally, we consider the extrapolation of Equation 15 to the mean halo mass of the bins (red symbols).

Our baseline analysis adopts the third method for bins 3-9, where we use the best fit of Equation 15 for each one, and the fourth method for bins 0-2, which are beyond the resolution limits of the FASTPM mocks and hence, we cannot apply the third method directly.

We present the results of our comparison in panel (b) of Figure 10, which shows the PNG bias parameter  $p$  as a function of  $M_{\text{halo}}$  for the different methods of estimating the power spectrum variance described above. For bins 0–3, we do not have enough mass resolution with the FASTPM mocks, so only results assuming the standard variances and the extrapolation of  $\sigma_F(P(k))$  are shown. Regardless of the method used to estimate the variance, we recover the same results within  $1\sigma$ . Moreover, the FASTPM approach is more accurate than the standard approach as it considers the fixed initial conditions in our simulations. Additionally, the best fit of  $\sigma_F(P(k))/P(k)$  provides almost the same results compared to using the extrapolation method. These results are consistent with using the variances directly obtained from FASTPM mocks, even considering their small error bars. While we cannot test and compare our fitting procedure outside the mass domain of the FASTPM mocks, we remark that our results are still consistent within  $1\sigma$  with the standard approach for all mass bins.

We now consider the fit to mass bins 0-9. We performed a linear fit on  $p$  and found that it is consistent with being a constant, confirming the results of Section 5.4. Furthermore, the weighted average yields  $p(\sigma_{S+M}) = 0.950 \pm 0.056$  and  $p(\text{direct FASTPM } \sigma_{F+M}) = 0.937 \pm 0.021$ , which agrees within  $1\sigma$  with our fiducial choice.

## 8. Constraining $f_{\text{NL}}$ with priors on $p$

In this section, we study how setting a prior in  $p$  (or equivalently, on  $b_\phi$ ) affects the constraints on  $f_{\text{NL}}$ . This is because, with the scale-dependent bias, we are only sensitive to the product  $b_\phi f_{\text{NL}}$ .

Here, we assume a Gaussian prior for  $p$  centred on  $p_{\text{prior}}$  and with a width  $\sigma(p)$ . To implement the priors in our MCMC procedure (see Section 5.1 for details), we modify the Gaussian likelihood by introducing this a second term in  $\chi^2$ :

$$\chi^2 = \sum_{i=0}^{N_k} \frac{(P_{\text{halos}}(k_i) - P_{\text{model}}(k_i, b_\phi, f_{\text{NL}}, b_1))^2}{\sigma^2(P(k_i))} + \frac{(p - p_{\text{prior}})^2}{\sigma^2(p)}. \quad (24)$$

In Section 8.1, we demonstrate how increasing the prior width  $\sigma(p)$  deteriorates the constraints in  $f_{\text{NL}}$ . In Section 8.2, we show how using these priors can affect the measurement of  $f_{\text{NL}}$  in future cosmological surveys.



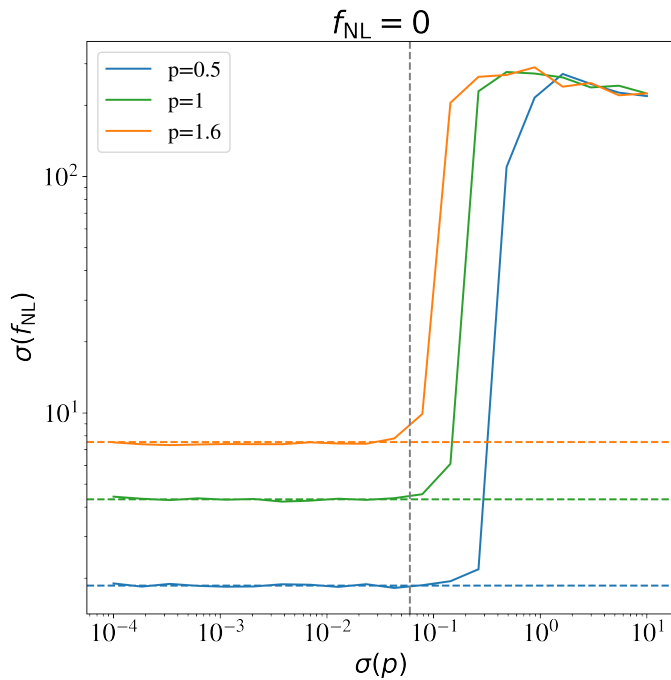


**Fig. 11.** Statistical error in  $f_{\text{NL}}$  as a function of the size of the prior on  $p$ , for three values for  $p$ , shown in different colours, as indicated in the legend. The mock data vector for this figure is generated using the linear power spectrum computed with CAMB in Equation 11 and fixing  $b_1 = 1.4$  and  $f_{\text{NL, fid}} = 0$ . The horizontal dashed lines show the case where we performed the fits fixing  $p$  in the model to its corresponding fiducial value. The dashed vertical line displays the value of the error in  $p$ , obtained for halos with mass between  $5 \times 10^{11}$  and  $1 \times 10^{12} h^{-1} M_{\odot}$  (bin 4 in Table 3).

### 8.1. Effect of the prior size on $\sigma(f_{\text{NL}})$

This section examines how the width of the prior for  $p$  affects the determination of  $f_{\text{NL}}$ . Nine mock halo power spectra are generated based on Equation 11. CAMB is used to compute the matter power spectrum in each case. Three  $f_{\text{NL}}$  values are considered: 0,  $-12$ , and  $50$ , with  $b_1$  set to  $1.4$  for all cases. The choice of  $f_{\text{NL, fid 1}} = 0$  is motivated by the current tightest constraint for  $f_{\text{NL}}$  by Planck Collaboration et al. (2020);  $f_{\text{NL, fid 1}} = -12$  and  $f_{\text{NL, fid 3}} = 50$  are motivated by two recent constraints coming from galaxy clustering analysis (Mueller et al. 2022; Rezaie et al. 2024). The values of  $b_{\phi}$  are derived in each case from Equation 13, assuming that  $p$  is  $0.5$ ,  $1$ , and  $1.6$ . MCMC analyses are conducted to measure  $f_{\text{NL}}$  and its uncertainty  $\sigma(f_{\text{NL}})$  for each of the nine mocks.

We analyse the data in two ways. First, we fix  $p$  to its fiducial value, assuming perfect knowledge of this quantity. Second, we allow  $p$  to vary, introducing a Gaussian prior centred on the fiducial value of  $p$  with a varying width. The idealised scenario of having a fixed  $p$ , has only two free parameters:  $b_1$  and  $f_{\text{NL}}$ . This scenario yields the most stringent constraints. Allowing  $p$  to vary requires a prior on this parameter to counter the degeneracy between  $p$  and  $f_{\text{NL}}$ . This is further discussed below.

In Figure 11, we show the uncertainty  $\sigma(f_{\text{NL}})$  for the setup described above as a function of the width of the prior in  $p$ ,  $\sigma(p)$ , for the case of  $f_{\text{NL}} = 0$ . The analysis for the three fiducial  $p$  values are shown in different colours. The values of  $\sigma(f_{\text{NL}})$  from assuming fixed values for  $p$  are shown as horizontal dashed lines. Those assuming a prior in  $p$  are shown as solid lines.

Figure 11 shows that constraints on  $f_{\text{NL}}$  are similar when considering either a fixed value of  $p$  or a prior, as long as this prior is narrow enough,  $\sigma(p) \lesssim 0.1$ . Beyond this threshold, the constraints weaken significantly, increasing in  $\sigma(f_{\text{NL}})$ . As we can see in Figure 11, this threshold depends on the fiducial value of  $p$ . In fact, it also depends on  $b_1$  and  $b_{\phi}$ . For a fixed  $b_1$ , the lower the  $p$  (and hence the higher the  $b_{\phi}$ ), the tighter the constraints on  $f_{\text{NL}}$ . In Figure 11 we only show results for  $f_{\text{NL}} = 0$ , but similar trends are found for  $f_{\text{NL}} = -12$  and  $50$ .

### 8.2. Forecast for a DESI-like survey

We go on to study the impact on the determination of  $f_{\text{NL}}$  in the context of current galaxy surveys when assuming either the universality relation or considering priors for  $p$  (or  $b_{\phi}$ ). We base our forecast on the clustering of the typical halos hosting cosmological tracers.

For this forecast, we assume survey properties similar to DESI, whose footprint will cover an area in the sky of  $\sim 14\,000 \text{ deg}^2$  (DESI Collaboration et al 2023). We consider the three cosmological tracers targeted by the DESI dark-time programme: luminous red galaxies (LRGs), emission-line galaxies (ELGs) and quasars (QSOs). For our analysis, we use the results given in Yu et al. (2024) for the DESI early data release (EDR), as they are based on the authors' analysis on the Gaussian UNIT simulation. Yu et al. found that DESI EDR LRGs, ELGs, and QSOs populate halos with typical masses of  $\log_{10}(M_{\text{halo, LRG}}) = 13.16$ ,  $\log_{10}(M_{\text{halo, ELG}}) = 11.90$ , and  $\log_{10}(M_{\text{halo, QSO}}) = 12.66$ , respectively. These masses correspond to our halo mass bins 8, 4, and 6, respectively (see Table 3). Additionally, each tracer is restricted to a certain range of redshifts. The redshift range for LRGs is from  $z = 0.4$  to  $z = 1.1$ , with an effective redshift of  $z_{\text{eff LRG}} = 0.814$ . For ELGs, the range goes from  $z = 0.8$  to  $z = 1.6$  with an effective redshift of  $z_{\text{eff ELG}} = 1.202$ . And for QSOs, we have considered the range from  $z = 0.8$  to  $z = 2.5$  with an effective redshift of  $z_{\text{eff QSO}} = 1.741$ . We computed each tracer's total volume, assuming a spherical shell between the redshift ranges and the entire DESI footprint. In this way, we get  $V_{\text{tot, LRG}} = 19.45 h^{-1} \text{Gpc}$ ,  $V_{\text{tot, ELG}} = 34.37 h^{-1} \text{Gpc}$ , and  $V_{\text{tot, QSO}} = 64.94 h^{-1} \text{Gpc}$ . The number densities Yu et al. found for the considered redshift range are  $n_{\text{LRG}} = 5.50 \times 10^{-4} h^3 \text{Mpc}^{-3}$ ,  $n_{\text{ELG}} = 7.26 \times 10^{-4} h^3 \text{Mpc}^{-3}$  and  $n_{\text{QSO}} = 2.4 \times 10^{-5} h^3 \text{Mpc}^{-3}$ . For the linear bias we assume  $b_{1, \text{LRG}} = 1.2/D(z)$ ,  $b_{1, \text{ELG}} = 0.84/D(z)$ , and  $b_{1, \text{QSO}} = 1.2/D(z)$ , where  $D(z)$  is the growth factor (DESI Collaboration et al. 2016; DESI Collaboration et al 2023). At the effective redshifts of interest, this leads to  $b_{1, \text{ELG}} = 1.503$ ,  $b_{1, \text{LRG}} = 2.568$ , and  $b_{1, \text{QSO}} = 2.628$ .

We generated the mock halo power spectrum using CAMB in Equation 11. As described in the previous section, here we consider three fiducial values for  $f_{\text{NL}}$ :  $f_{\text{NL, fid 1}} = 0$ ,  $f_{\text{NL, fid 2}} = -12$ , and  $f_{\text{NL, fid 3}} = 50$ . Regarding  $b_{\phi}$ , we assume it follows the form given by Equation 13. We use the values of  $p$  measured in this work for the mass bin corresponding to each tracer<sup>10</sup>:  $p_{\text{LRG}} = 1.11 \pm 0.27$ ,  $p_{\text{ELG}} = 0.895 \pm 0.055$  and  $p_{\text{QSO}} = 0.973 \pm 0.077$ . The minimum wavenumber considered for the power spectrum is given by the fundamental wavenumber,  $k_{\text{min, tracer}} = 2\pi/V_{\text{tot, tracer}}^{1/3}$ . The corresponding covariance is calculated using Equation 14,

<sup>10</sup> This is an assumption for the forecast in order to understand and highlight the impact of priors that PNG-UNITsims is able to set. However, we expect that redshift evolution and galaxy formation could modify the value of  $p$ , and we expect to tackle these in detail in follow-up studies.

**Table 4.** Forecasts on  $f_{\text{NL}}$  for halos hosting the different tracers targeted by DESI.

	ELG hosts			LRG hosts			QSO hosts	
	$p = 1$	$p_{\text{fid}} = 0.895$	prior	$p = 1$	$p_{\text{fid}} = 1.11$	prior	$p = 1$	prior
$f_{\text{NL}}^{\text{fid}} = 0$	$-0.3 \pm 3.4$	$0.0 \pm 2.9$	$-0.2 \pm 2.9$	$-0.2 \pm 3.0$	$-0.3 \pm 3.1$	$-0.5 \pm 3.4$	$-0.3 \pm 3.3$	$-0.5 \pm 3.3$
$f_{\text{NL}}^{\text{fid}} = -12$	$-15.1 \pm 3.3$	$-12.5 \pm 2.7$	$-12.7 \pm 2.9$	$-11.4 \pm 2.3$	$-12.4 \pm 2.3$	$-13.0 \pm 3.1$	$-11.9 \pm 3.7$	$-12.1 \pm 3.4$
$f_{\text{NL}}^{\text{fid}} = 50$	$60.4 \pm 5.5$	$50.0 \pm 4.5$	$50.3 \pm 5.7$	$46.1 \pm 4.8$	$49.7 \pm 4.9$	$51.5 \pm 9.1$	$50.8 \pm 3.5$	$50.3 \pm 3.8$

**Notes.** In the three sections of the table, we fix the fiducial values of  $p$  to the values we find in Table 3 for the halos with masses similar to those that host ELGs, LRGs and QSOs in Yuan et al. (2024) (bin 4, bin 8, and bin 6) respectively. We also consider three fiducial  $f_{\text{NL}}$  values, as listed in each of the three rows. In the first for each tracer, we assume  $p = 1$  and we fix  $b_\phi$  using Equation 13. In the second column, labeled as  $p_{\text{fid}}$ , we conduct the fitting in the same way, but we fix  $p$  to the fiducial value for each sample. Finally, in the prior columns, we use our results for  $p$  to conduct the fits with  $p = 0.895 \pm 0.055$ ,  $p = 1.11 \pm 0.27$ , and  $p = 0.973 \pm 0.077$  for the ELG, LRG, and QSO-like samples, respectively.

considering the survey parameters described above for each tracer.

We used an MCMC fitting procedure to determine the impact on the measurement of  $f_{\text{NL}}$  from assuming a prior for  $p$  or not. We employed the same methodology as for our main results. In this analysis, all the cosmological parameters are fixed, except for  $b_1$ ,  $f_{\text{NL}}$ , and  $b_\phi$ . When fixing  $b_\phi$  to the universality relation value, we defined the value of  $\chi^2$  using Equation 18. When considering  $p$  as a free parameter, we incorporated a Gaussian prior centred on  $p_{\text{LRG}}$ ,  $p_{\text{ELG}}$  and  $p_{\text{QSO}}$  for each case value and a width given by our errors. In this case,  $\chi^2$  is defined by Equation 24.

In Table 4, we summarise our findings. Fixing  $p$  to the universality relation induce a bias of  $1.9\sigma$  for  $f_{\text{NL}}^{\text{fid}} = 50$  and  $0.9\sigma$  for  $f_{\text{NL}}^{\text{fid}} = -12$  for ELGs. These biases arise because the halos hosting ELGs have a value for  $p$  below one by  $\sim 10\%$ . For LRGs, we also find a  $0.8\sigma$  difference for the case with  $f_{\text{NL}}^{\text{fid}} = 50$ . Finally, for the QSO hosts, we correctly recovered the fiducial values of  $f_{\text{NL}}$  given that the value of  $p$  for this sample is consistent with  $p = 1$ .

When we fix  $p = p_{\text{fid}}$ , we recovered unbiased results for  $f_{\text{NL}}$  as expected. Nevertheless, the errors in  $f_{\text{NL}}$  increase or decrease if  $p_{\text{fid}}$  is higher or lower compared to the case with  $p = 1$ . These are the cases of the ELG hosts and LRG hosts, respectively. This variation in  $\sigma(f_{\text{NL}})$  is because the larger  $b_\phi$  is, the tighter the constraints on  $f_{\text{NL}}$  are, as we are only sensitive to the product of both quantities. We found negligible differences for the QSO hosts.

Finally, we recovered unbiased results for the three tracers when using our priors while, at the same time, the constraining power is comparable to fixing  $p$  to its fiducial value. In the case of the ELG hosts, our constraints are equal for  $f_{\text{NL}}^{\text{fid}} = 0$ , deteriorating by 7% and a 27% for  $f_{\text{NL}}^{\text{fid}} = -12$ , and  $f_{\text{NL}}^{\text{fid}} = 50$ , respectively. For the LRG hosts, our priors perform worse, deteriorating the constraints by a 9%, a 34% and a 85% for  $f_{\text{NL}}^{\text{fid}} = 0$ ,  $f_{\text{NL}}^{\text{fid}} = -12$ , and  $f_{\text{NL}}^{\text{fid}} = 50$ , respectively. Nevertheless, we are still able to constrain  $f_{\text{NL}}$  without recovering the degeneration between this parameter and  $p$ . Finally, our priors for the QSO hosts are comparable to fixing  $p = 1$ , providing even tighter constraints for  $f_{\text{NL}}^{\text{fid}} = -12$ .

## 9. Summary and conclusions

Detecting primordial non-Gaussianities (PNG) would have a major impact on how we understand inflation. The key to measuring or accurately constraining PNG in the near future is to understand the scale-dependent bias parameter,  $b_\phi$ , and how it varies for different cosmological tracers.

In this paper, we study the scale-dependent bias  $b_\phi$  for dark matter halos with masses from  $2 \times 10^{10} h^{-1} M_\odot$  to  $5 \times 10^{14} h^{-1} M_\odot$ .

To achieve this, we have developed PNG-UNIT, a new full N-body simulation with local non-Gaussian initial conditions ( $f_{\text{NL}} = 100$ ). PNG-UNIT is the largest simulation to date that incorporates non-Gaussian initial conditions. The simulation has  $4096^3$  dark matter particles in a  $1 (h^{-1} \text{Gpc})^3$  box, which was run using the L-GADGET2 code. The cosmology of the simulation is based on Planck Collaboration et al. (2016) (see Table 1). PNG-UNIT assumes local PNG with an amplitude of  $f_{\text{NL}} = 100$ . We have chosen a large value of  $f_{\text{NL}}$  to increase the signal from PNG while reducing the errors on  $b_\phi$ . We significantly reduced the error on  $b_\phi$  by using the method proposed in Avila & Adame (2023) for simulations with fixed-and-matched initial conditions. The amplitudes of the modes in the initial conditions are fixed to their expectation values, and the phases are matched to one of the realisations of the Gaussian UNIT simulations (Chuang et al. 2019), following Avila & Adame (2023).

In addition to the main simulation, PNG-UNIT, we also developed supporting simulations: a set of full N-body simulations, either with lower resolution or smaller volumes than PNG-UNIT, along with 100 fast mocks, half of which have  $f_{\text{NL}} = 100$  and the other half with  $f_{\text{NL}} = 0$ , generated with the approximated method FASTPM. We refer to the whole set of simulations as PNG-UNITsims.

The PNG-UNITsims suite (see Section 3.2) is a unique laboratory for studying galaxy clustering models in the presence of local PNGs. The simulations in this suite have effective volumes comparable to current spectroscopic galaxy surveys. The reference simulation, PNG-UNIT, has a mass resolution high enough to accurately resolve the dark matter halos expected to host the galaxies currently targeted by surveys such as DESI and EUCLID. Thus, the PNG-UNITsims suite is a powerful tool to develop and test analysis pipelines to measure  $f_{\text{NL}}$  with current spectroscopic galaxy surveys.

In this first study of the PNG-UNITsims suite, we were able to constrain the non-Gaussian bias parameter  $b_\phi$  using mass-selected samples of dark matter halos. We inferred the scale-dependent bias from the halo power spectrum measured for the Gaussian and the non-Gaussian simulations. From the power spectra, we inferred  $b_1$  and  $b_\phi f_{\text{NL}}$  and correlated the measurements in both simulations Section 5. Moreover, given that we know the input values of  $f_{\text{NL}}$ , we can derive  $b_\phi$  or  $p$ . Our findings can be summarised as follows:

- We measured  $b_\phi f_{\text{NL}}$  using the fix-and-match technique (§4.3) by combining the information of the Gaussian and the non-Gaussian simulation. This technique allows us to cancel out much of the cosmic variance (§5.2).
- By assuming the universality relation, we recovered the input values of  $f_{\text{NL}}$  for our simulations within  $1\sigma$  for halos between  $1 \times 10^{12} h^{-1} M_\odot$  and  $1 \times 10^{14} h^{-1} M_\odot$ . The power spectra

are very noisy for higher halo masses due to their low number densities. As the variance estimates are not robust for these massive halos, we have not included them in the rest of our analyses.

- For halos with masses between  $5 \times 10^{10} h^{-1} M_{\odot}$  and  $1 \times 10^{12} h^{-1} M_{\odot}$  we find deviations from the input value of  $f_{\text{NL}} = 100$ , which reaches a significance of  $4\sigma$  for halos between  $1 \times 10^{11} h^{-1} M_{\odot}$  and  $2 \times 10^{11} h^{-1} M_{\odot}$ , suggesting that the value of  $p$  assumed ( $p = 1$ ) does not accurately describe the clustering of these halos.
- We measured  $p$  by fixing  $f_{\text{NL}}$  to the input values. For halos with masses higher than  $1 \times 10^{12} h^{-1} M_{\odot}$  and between  $2 \times 10^{10} h^{-1} M_{\odot}$  and  $5 \times 10^{10} h^{-1} M_{\odot}$ , we find  $p$  to be consistent with the universality relation. For halos with masses between  $5 \times 10^{10} h^{-1} M_{\odot}$  and  $1 \times 10^{12} h^{-1} M_{\odot}$ , we find  $p$  to be  $\sim 10\%$  below the universality relation, with a significance between  $1.5\sigma$  and  $3.1\sigma$ .
- Combining the information of  $b_{\phi} f_{\text{NL}}$  from mass bins 0–9 ( $M_{\text{halo}}$  between  $2 \times 10^{10} h^{-1} M_{\odot}$  and  $5 \times 10^{13} h^{-1} M_{\odot}$ ) we find a preferred value of  $p = 0.955 \pm 0.013$  (68% c.l.). This result is more than  $3\sigma$  away from the universality relation (i.e.  $p = 1$ ).

We assured the validity of our results for  $M_{\text{halo}} \gtrsim 2 \times 10^{10} h^{-1} M_{\odot}$  by checking that the convergence with the LR-UNIT simulations (2048<sup>3</sup>) occur at  $M_{\text{halo}} \sim 20m_{\text{part}}$ . Moreover, we also made a comparison with the separate universe technique, but the priors reported by the PNG-UNIT simulation are more robust. For the set-up considered here, we find that the separate universe tends to underestimate the uncertainty reported on  $b_{\phi}$ . By looking at the scatter and lack of convergence of the separate universe results, we also conclude that the uncertainty associated with those  $b_{\phi}$  measurements would be larger than the one found by PNG-UNITsims.

We explored how this affects variations on the mass definition used for the mass cuts to the measurements of  $p$ , finding consistency for all mass definitions except for  $M_{500c}$  (§6.3). We argue that  $b_{\phi}$  might not depend only on the halo mass through  $b_1$  but also on other parameters. We leave a more detailed exploration of these dependencies for future work.

We have also tested the robustness of the above results to variations in the choice of the scale cuts (§7.1) and the way we compute the variances of the power spectrum (§7.2). None of the above is shown to have a significant impact.

Finally, we construct priors on the scale-dependent bias for DESI galaxies based on the simplified assumption that those tracers can be identified directly by the mass of their host halo at  $z = 1$ . We show that these priors are:

1. required to get unbiased constraints on  $f_{\text{NL}}$  (compared to the universality relation that may bias the results, up to  $2\sigma$  for the setup considered);
2. sufficiently tight to allow us to constrain  $f_{\text{NL}}$  with DESI at a comparable precision with respect to cases where  $p$  is fixed to the fiducial value.

All these results show the capability of the PNG-UNITsims suite as a valuable tool for interpreting observations with DESI and EUCLID. Specifically, we address the issue of putting priors on  $b_{\phi}$ . While we have analysed how the halo power spectrum can be used to constrain the scale-dependent bias in this work, the PNG-UNITsims suite is a unique tool to test and develop alternative methods for constraining PNG with cosmological surveys. In the future, we plan to include galaxies in our simulations and consider other clustering statistics such as the

configuration space correlation functions, higher order statistics including the bispectrum or trispectrum, and one-point statistics such as counts-in-cells, density peaks, and galaxy cluster counts.

## Data Availability

The halo catalogues used in this paper are available through the UNITsIM website: <http://www.unitsims.org/> The other data products will be shared under email request to the corresponding author.

*Acknowledgements.* We thank V. Yankelevich, O. Hahn, M. Manera, and R. Scoccimarro for the valuable discussions on how to solve some early problems with initial conditions. We thank the Benasque science center for fostering useful discussions regarding this work. This work has been supported by Ministerio de Ciencia e Innovación (MICINN) under the following research grants: PID2021-122603NB-C21 (AGA, VGP, GY and AK), PID2021-123012NB-C41 (SA) and PID2021-123012NB-C43 (JGB). AK further thanks Embrace for ‘gravity’. SA and VGP have been or are supported by the Atracción de Talento Contract no. 2019-T1/TIC-12702 granted by the Comunidad de Madrid in Spain. JGB has also been supported by the Centro de Excelencia Severo Ochoa Program CEX2020-001007-S at IFT. IFAE is partially funded by the CERCA program of the Generalitat de Catalunya. The PNG-UNIT simulation has been run thanks to the computer resources at MareNostrum granted by the Red Española de Supercomputación and the technical support provided by Barcelona Supercomputing Center (RES-AECT-2021-3-0004, RES-AECT-1-0007, RES-AECT-2022-3-0030, RES-AECT-2023-1-0014, and RES-AECT-2023-2-0006.).

## References

- Alam, S., de Mattia, A., Tamone, A., et al. 2021, *Monthly Notices of the Royal Astronomical Society*, 504, 4667
- Angulo, R. E. & Pontzen, A. 2016, *Monthly Notices of the Royal Astronomical Society: Letters*, 462, L1
- Avila, S. & Adame, A. G. 2023, *Monthly Notices of the Royal Astronomical Society*, 519, 3706
- Avila, S., Crocce, M., Ross, A. J., et al. 2018, *Monthly Notices of the Royal Astronomical Society*, 479, 94
- Avila, S., Gonzalez-Perez, V., Mohammad, F. G., et al. 2020, *Monthly Notices of the Royal Astronomical Society*, 499, 5486
- Avila, S., Vos-Ginés, B., Cunnington, S., et al. 2021, *Monthly Notices of the Royal Astronomical Society*, 510, 292
- Bacon, D. J., Battye, R. A., Bull, P., et al. 2020, *Publications of the Astronomical Society of Australia*, 37
- Baldauf, T., Seljak, U., Senatore, L., & Zaldarriaga, M. 2016, *Journal of Cosmology and Astroparticle Physics*, 2016, 007–007
- Bardeen, J. M., Bond, J. R., Kaiser, N., & Szalay, A. S. 1986, *ApJ*, 304, 15
- Barreira, A. 2022a, *Journal of Cosmology and Astroparticle Physics*, 2022, 013
- Barreira, A. 2022b, *Journal of Cosmology and Astroparticle Physics*, 2022, 057
- Barreira, A. 2022c, *Journal of Cosmology and Astroparticle Physics*, 2022, 033
- Barreira, A., Cabass, G., Schmidt, F., Pillepich, A., & Nelson, D. 2020, *Journal of Cosmology and Astroparticle Physics*, 2020, 013
- Baumann, D., Jackson, M. G., Adshead, P., et al. 2009, in *AIP Conference Proceedings (AIP)*
- Behroozi, P. S., Wechsler, R. H., & Wu, H.-Y. 2012, *The Astrophysical Journal*, 762, 109
- Biagetti, M., Lazeyras, T., Baldauf, T., Desjacques, V., & Schmidt, F. 2017, *Monthly Notices of the Royal Astronomical Society*, 468, 3277
- Bryan, G. L. & Norman, M. L. 1998, *The Astrophysical Journal*, 495, 80
- Byrnes, C. T. & Choi, K.-Y. 2010, *Advances in Astronomy*, 2010, 1
- Cabass, G., Ivanov, M. M., Philcox, O. H., Simonović, M., & Zaldarriaga, M. 2022, *Physical Review D*, 106
- Castorina, E., Hand, N., Seljak, U., et al. 2019, *Journal of Cosmology and Astroparticle Physics*, 2019, 010
- Chan, K. C., Ferrero, I., Avila, S., et al. 2022, *Monthly Notices of the Royal Astronomical Society*, 511, 3965
- Chartier, N., Wandelt, B., Akrami, Y., & Villaescusa-Navarro, F. 2021, *Monthly Notices of the Royal Astronomical Society*, 503, 1897
- Chuang, C.-H., Yepes, G., Kitaura, F.-S., et al. 2019, *Monthly Notices of the Royal Astronomical Society*, 487, 48
- Cochrane, R. K., Best, P. N., Sobral, D., et al. 2017, *Monthly Notices of the Royal Astronomical Society*, 469, 2913
- Coulton, W. R., Villaescusa-Navarro, F., Jamieson, D., et al. 2023, *The Astrophysical Journal*, 943, 64

- Cremineilli, P. & Zaldarriaga, M. 2004, *Journal of Cosmology and Astroparticle Physics*, 2004, 006
- Crocce, M., Pueblas, S., & Scoccimarro, R. 2006, *MNRAS*, 373, 369
- Crocce, M., Pueblas, S., & Scoccimarro, R. 2012, *LPTIC: 2nd-order Lagrangian Perturbation Theory Initial Conditions*, *Astrophysics Source Code Library*, record ascl:1201.005
- Dalal, N., Doré, O., Huterer, D., & Shirokov, A. 2008, *Physical Review D*, 77
- DeRose, J., Chen, S.-F., Kokron, N., & White, M. 2023, *Journal of Cosmology and Astroparticle Physics*, 2023, 008
- DESI Collaboration, Aghamousa, A., Aguilar, J., et al. 2016, *The DESI Experiment Part I: Science, Targeting, and Survey Design*
- DESI Collaboration et al. 2023, *The Early Data Release of the Dark Energy Spectroscopic Instrument*
- Desjacques, V., Jeong, D., & Schmidt, F. 2018, *Physics Reports*, 733, 1
- Desjacques, V., Seljak, U., & Iliev, I. T. 2009, *Monthly Notices of the Royal Astronomical Society*, 396, 85
- Ding, Z., Chuang, C.-H., Yu, Y., et al. 2022, *Monthly Notices of the Royal Astronomical Society*, 514, 3308
- Ezquiaga, J. M., García-Bellido, J., & Vennin, V. 2023, *Phys. Rev. Lett.*, 130, 121003
- Feldman, H. A., Kaiser, N., & Peacock, J. A. 1994, *The Astrophysical Journal*, 426, 23
- Feng, Y., Chu, M.-Y., Seljak, U., & McDonald, P. 2016, *Monthly Notices of the Royal Astronomical Society*, 463, 2273
- Fondi, E., Verde, L., Villaescusa-Navarro, F., et al. 2024, *Journal of Cosmology and Astroparticle Physics*, 2024, 048
- Foreman-Mackey, D., Hogg, D. W., Lang, D., & Goodman, J. 2013, *Publications of the Astronomical Society of the Pacific*, 125, 306
- Giannantonio, T. & Percival, W. J. 2014, *Monthly Notices of the Royal Astronomical Society: Letters*, 441, L16–L20
- Giannantonio, T., Porciani, C., Carron, J., Amara, A., & Pillepich, A. 2012, *Monthly Notices of the Royal Astronomical Society*, 422, 2854
- Gonzalez-Perez, V., Comparat, J., Norberg, P., et al. 2018, *MNRAS*, 474, 4024
- Grossi, M., Verde, L., Carbone, C., et al. 2009, *Monthly Notices of the Royal Astronomical Society*, 398, 321
- Hadzhiyska, B., Garrison, L., Eisenstein, D. J., & Ferraro, S. 2024, *AbacusPNG: A modest set of simulations of local-type primordial non-Gaussianity in the DESI era*
- Hamaus, N., Seljak, U., & Desjacques, V. 2011, *Physical Review D*, 84
- Hand, N., Feng, Y., Beutler, F., et al. 2018, *The Astronomical Journal*, 156, 160
- Ho, S., Agarwal, N., Myers, A. D., et al. 2015, *Journal of Cosmology and Astroparticle Physics*, 2015, 040
- Hockney, R. W. & Eastwood, J. W. 1981, *Computer Simulation Using Particles*
- Kaiser, N. 1984, *ApJ*, 284, L9
- Klypin, A., Yepes, G., Gottlöber, S., Prada, F., & Heß, S. 2016, *Monthly Notices of the Royal Astronomical Society*, 457, 4340
- Knebe, A., Lopez-Cano, D., Avila, S., et al. 2022, *Monthly Notices of the Royal Astronomical Society*, 510, 5392
- Kokron, N., Chen, S.-F., White, M., DeRose, J., & Maus, M. 2022, *Journal of Cosmology and Astroparticle Physics*, 2022, 059
- Komatsu, E. & Spergel, D. N. 2001, *Phys. Rev. D*, 63, 063002
- Kopana, M., Jolicœur, S., & Maartens, R. 2024, *European Physical Journal C*, 84, 491
- Laureijs, R., Amiaux, J., Arduini, S., et al. 2011, *arXiv e-prints*, arXiv:1110.3193
- Lazeyras, T., Barreira, A., Schmidt, F., & Desjacques, V. 2023, *Journal of Cosmology and Astroparticle Physics*, 2023, 023
- Lazeyras, T. & Schmidt, F. 2018, *Journal of Cosmology and Astroparticle Physics*, 2018, 008
- Leistedt, B., Peiris, H. V., & Roth, N. 2014, *Physical Review Letters*, 113
- Lewis, A., Challinor, A., & Lasenby, A. 2000, *The Astrophysical Journal*, 538, 473
- LoVerde, M., Miller, A., Shandera, S., & Verde, L. 2008, *Journal of Cosmology and Astroparticle Physics*, 2008, 014
- LSST Science Collaboration, Abell, P. A., Allison, J., et al. 2009, *arXiv e-prints*, arXiv:0912.0201
- Lucie-Smith, L., Barreira, A., & Schmidt, F. 2023, *Monthly Notices of the Royal Astronomical Society*, 524, 1746–1756
- Lyth, D. H., Ungarelli, C., & Wands, D. 2003, *Phys. Rev. D*, 67, 023503
- Maion, F., Angulo, R. E., & Zennaro, M. 2022, *Journal of Cosmology and Astroparticle Physics*, 2022, 036
- Maldacena, J. 2003, *Journal of High Energy Physics*, 2003, 013
- Manera, M., Scoccimarro, R., Percival, W. J., et al. 2012, *Monthly Notices of the Royal Astronomical Society*, 428, 1036
- Matarrese, S. & Verde, L. 2008, *The Astrophysical Journal*, 677, L77
- Matarrese, S., Verde, L., & Jimenez, R. 2000, *The Astrophysical Journal*, 541, 10
- Mueller, E.-M., Percival, W. J., & Ruggeri, R. 2018, *Monthly Notices of the Royal Astronomical Society*, 485, 4160–4166
- Mueller, E.-M., Rezaie, M., Percival, W. J., et al. 2022, *Monthly Notices of the Royal Astronomical Society*, 514, 3396
- Nishimichi, T., Taruya, A., Koyama, K., & Sabiu, C. 2010, *Journal of Cosmology and Astroparticle Physics*, 2010, 002–002
- Pajer, E., Schmidt, F., & Zaldarriaga, M. 2013, *Physical Review D*, 88
- Pillepich, A., Porciani, C., & Hahn, O. 2009, *Monthly Notices of the Royal Astronomical Society*, 402, 191
- Planck Collaboration, Ade, P. A. R., Aghanim, N., et al. 2016, *Astronomy & Astrophysics*, 594, A13
- Planck Collaboration, Akrami, Y., Arroja, F., et al. 2020, *A&A*, 641, A9
- Prada, F., Ereza, J., Smith, A., et al. 2023, *arXiv e-prints*, arXiv:2306.06315
- Reyes-Peraza, G., Avila, S., Gonzalez-Perez, V., et al. 2024, *MNRAS*, 529, 3877
- Rezaie, M., Ross, A. J., Seo, H.-J., et al. 2024, *MNRAS[arXiv:2307.01753]*
- Riquelme, W. et al. 2023, *Mon. Not. Roy. Astron. Soc.*, 523, 603
- Rocher, A., Ruhlmann-Kleider, V., Burtin, E., et al. 2023, *J. Cosmology Astropart. Phys.*, 2023, 016
- Ross, A. J., Banik, N., Avila, S., et al. 2017, *Monthly Notices of the Royal Astronomical Society*, 472, 4456
- Ross, A. J., Percival, W. J., Carnero, A., et al. 2012, *Monthly Notices of the Royal Astronomical Society*, 428, 1116
- Rossi, G., Choi, P. D., Moon, J., et al. 2020, *Monthly Notices of the Royal Astronomical Society*
- Salopek, D. S. & Bond, J. R. 1990, *Phys. Rev. D*, 42, 3936
- Sartoris, B., Biviano, A., Fedeli, C., et al. 2016, *Monthly Notices of the Royal Astronomical Society*, 459, 1764
- Scoccimarro, R., Hui, L., Manera, M., & Chan, K. C. 2012, *Physical Review D*, 85
- Slosar, A., Hirata, C., Seljak, U., Ho, S., & Padmanabhan, N. 2008, *Journal of Cosmology and Astroparticle Physics*, 2008, 031
- Springel, V. 2005, *Monthly Notices of the Royal Astronomical Society*, 364, 1105
- Springel, V., White, S. D. M., Jenkins, A., et al. 2005, *Nature*, 435, 629
- Sullivan, J. M., Pridon, T., & Seljak, U. 2023, *Journal of Cosmology and Astroparticle Physics*, 2023, 004
- Tinker, J. L., Robertson, B. E., Kravtsov, A. V., et al. 2010, *The Astrophysical Journal*, 724, 878
- Villaescusa-Navarro, F., Naess, S., Genel, S., et al. 2018, *The Astrophysical Journal*, 867, 137
- Wagner, C. & Verde, L. 2012, *Journal of Cosmology and Astroparticle Physics*, 2012, 002
- Yamauchi, D., Takahashi, K., & Oguri, M. 2014, *Physical Review D*, 90
- Yu, J., Zhao, C., Gonzalez-Perez, V., et al. 2024, *MNRAS*, 527, 6950
- Yuan, S., Zhang, H., Ross, A. J., et al. 2024, *MNRAS*, 530, 947
- Zhao, C., Chuang, C.-H., Bautista, J., et al. 2021, *Monthly Notices of the Royal Astronomical Society*, 503, 1149